Simplified modeling of the impact of lithospheric-scale geological processes on thermal histories and low-temperature thermochronometers

Dawn A. Kellett[1,*] and David M. Whipp[2,*]

[1]Geological Survey of Canada-Atlantic, Natural Resources Canada, Dartmouth, B2Y 4A2, Canada
[2]Department of Geosciences and Geography, University of Helsinki, 00014 University of Helsinki, Helsinki, Finland
[*]These authors contributed equally to this work.

Correspondence: Dawn A. Kellett (dawn.kellett@nrcan-rncan.gc.ca)

Abstract. Many geological processes influence or perturb the thermal state of the lithosphere. This presents a challenge for relating thermal history data modeled from thermochronometers such as apatite and zircon fission-track and (U-Th)/He dating, to geological evolution, a primary goal of many thermochronology studies. Here we address this challenge by exploring the thermal and thermochronological evolution of tracked rock parcels ~~in~~ for a large set of 55-50 Ma 1D models that simulate key lithospheric geological processes, including erosional exhumation, sedimentary burial and exhumation, dip-slip faulting and delamination of the lithospheric mantle. We compare results from common depth history scenarios in which the Moho either experiences exhumation/burial or remains at a fixed depth balanced by crustal flux and erosion. Results show that Moho depth changes have a significant effect on thermal histories and thermochronometers, though this is not often considered in thermal history studies. Further, our results show that the recorded response of rock thermal histories/thermochronometers in the upper crust and geological processes that disrupt the crustal thermal field may be disassociated in time, because of the spatial origin, time and length scales of different heat transfer mechanisms. For example, a delamination event produces younger thermochronometer ages than an identical crustal exhumation history without delamination, but those young ages do not record the timing of delamination.

1 Introduction

Heat in the Earth's lithosphere is a complex process variable, and many geological processes influence or perturb the lithospheric geothermal gradient. The thermal evolution of the lithosphere is typically studied from surface samples that may have not only experienced a dynamic geothermal gradient but also changed position relative to the Earth's surface through geological time. Consequently, the relationship between the geological processes a rock has experienced on its path to the present and that rock's thermal history is of broad interest to the geological community.

Low-temperature thermochronology is a field of research in which the thermally controlled retention of radioactive decay products in geological materials is measured to reconstruct mineral and rock thermal histories, especially regarding their passage through the upper crust ($< 350°$ C). Such thermal histories are most often constructed by inverting low-temperature thermochronological data using software such as HeFTy (Ketcham, 2005) or QTQt (Gallagher, 2012) to identify envelopes of most likely thermal histories.

While such inversions of rock thermochronometer data are highly informative depictions of rock thermal histories, the ultimate goal of most low-temperature thermochronological studies is to relate thermal histories to geological processes, in order to reconstruct the tectonic and/or landscape evolution of the upper crust. This requires an ability to model the dynamic evolution of the lithospheric thermal field (e.g., Ehlers, 2005). Software for inverting thermal histories, such as HeFTy or QTQt, are user friendly, widely used, and sophisticated in their ability to address complex retention behaviors of the various low-temperature thermochronometers. Yet, the ability to relate those thermal histories to geological processes, described for example in Flowers et al. (2015) as stepping from "level 2 – thermal model outputs" to "level 3 – geological interpretation", remains a critical interpretive challenge.

There are a range of existing 2D and 3D surface process, kinematic and/or geodynamic modeling software packages available that solve the heat equation through time in response to geological processes such as faulting, fluvial erosion, or viscous crustal flow that can, or could be adapted to, forward model or invert thermochronometer age data, such as Pecube (Braun, 2003) or Badlands and Underworld (Salles and Hardiman, 2016; Mansour et al., 2020). However, these approaches are computationally expensive and require steep learning curves, presenting barriers to those in pursuit of simple parameter exploration.

In this contribution, we explore first-order relationships between the thermal evolution of the lithosphere and the thermochronological record using a new 1D modeling code with thermokinematic capabilities that bridges between the existing thermal history modeling tools and more complex 2D and 3D thermokinematic modeling software. The simplified relationships that we explore between rock thermochronometer ages, low-temperature thermal histories, and geological processes are aimed at improving our ability to make these relationships in more complex empirical studies. We consider an example set of 1D scenarios involving erosion, sedimentary burial, thrust and extensional faulting, and delamination of the lithospheric mantle. In these models, we examine the conditions under which thermal histories deviate from or track with depth histories, and how the resulting thermochronometer ages and time lags between thermochronometers relate to the geological process(es) triggering rock heating/cooling.

2 Methods

2.1 T_c1D: 1D heat transfer and thermochronometer age prediction model

T_c1D, the modeling software used in this study, is a 1D thermal and thermochronometer age prediction software package written in Python that simulates the dynamic thermal effects of common geological processes at the scale of the full lithosphere ~~(Whipp, 2022)~~(Whipp, 2022; Whipp et al., 2026). The software uses recorded thermal histories to calculate various thermochronometer ages for particles that reach the model surface during and at the end of simulations. The design of T_c1D is deliberately simple, allowing the user to vary a range of parameters and quickly explore their effects in (multi-)thermochronometry datasets. Thus, the goal is not to simulate all the geological details of a complex geodynamic process like lithospheric delamination or post-orogenic collapse, but rather to produce first-order dynamic "geological" heat transfer

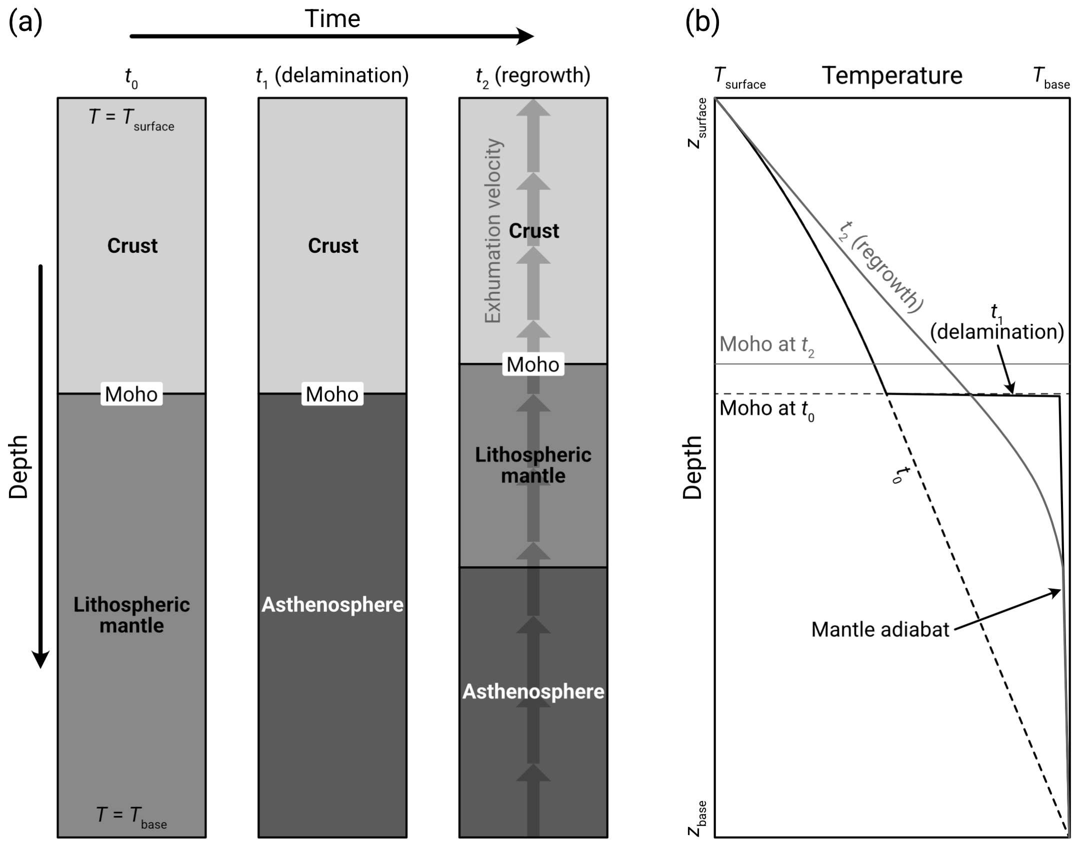

Figure 1. Schematic overview of the time evolution of an example $\mathrm{T_c}$1D model of lithospheric delamination and the corresponding geotherms. (a) Three lithospheric-scale columns representing the initial thermal solution (t_0, left), moment of instantaneous lithospheric delamination (t_1, center), and dynamic regrowth of mantle lithosphere millions of years after delamination (t_2, right). The thermal boundary conditions are constant through time (left), and erosional exhumation advects heat and the Moho toward the surface after delamination (right). (b) Geotherms for each of the three model stages showing the thermal effects of delamination and thermal advection.

models and explore the relationships between those models, the corresponding depth and thermal histories experienced by particles reaching the model surface, and calculated low-temperature thermochronometry ages and characteristics (Fig. 1). Thermochronometer systems supported in $\mathrm{T_c}$1D include apatite (U-Th)/He (AHe), apatite fission-track (AFT), zircon (U-Th)/He (ZHe), and zircon fission track (ZFT). A more complete description of $\mathrm{T_c}$1D, its design, and technical details can be found in Whipp et al. (2026).

$\mathrm{T_c}$1D uses the finite-difference method to solve the transient heat transfer equation in 1D in the crust and lithospheric mantle, including the thermal effects of advection and volumetric heat production. Temperatures are fixed at the surface and base of the model, and the initial thermal field is calculated at a steady state using an optional advection velocity specified for the start of the simulation. The temperature calculation forward in time from the initial state can use either an implicit or explicit finite-difference solution with user-defined time steps. Rock thermal and physical properties are defined separately for the crust, lithospheric mantle, and asthenosphere. A variety of erosion models are built into T_c1D allowing users to explore many different burial (i.e., negative erosion) and exhumation histories (see Sect. 2.2 for details).

Thermal histories are recorded by tracking the temperature of particles that reach the model surface at the end of the simulation, and optionally at specified intervals during the simulation. The thermal histories are used to predict thermochronometer ages using the radiation damage accumulation and annealing models for AHe (Flowers et al., 2009) and ZHe (Guenthner et al., 2013), and the fission track annealing models for AFT (Ketcham et al., 1999) and ZFT (van der Beek et al., 1995) using the kinetics of Tagami et al. (1998) or Rahn et al. (2004). The program used for AHe and ZHe age predictions is from Ketcham et al. (2018), the AFT age prediction program is from Ketcham et al. (2000) as implemented in Braun et al. (2012), and the ZFT age prediction code was ported to Python following its implementation in Braun et al. (2012).

2.2 T_c1D model design, assumptions, and considerations

As noted above, all T_c1D models begin from an initial conductive thermal steady state. In some of the model scenarios presented in this work, additional time at the thermal steady state (e.g., 5 Myr) is included in the design in order to highlight the onset of changes in the thermal history that result from various geological processes. For example, when processes such as the onset of faulting or heating due to removal of the mantle lithosphere are included, additional time at the start of the simulation is included in order to clearly show the timing of the changes in the recorded temperatures following the onset of such processes.

The durations of the models in this work are all $\sim$50 Myr to account for both times during which tectonic activity occurs and post-tectonic erosional exhumation. Although this may be a longer duration than recorded in thermochronometer data from active tectonic settings today, such as the Himalaya or Southern Alps of New Zealand, these generic models can be used as templates that can be modified to explore "younger" regions. To aid in supporting this, two examples of "younger" activity are provided in the supplementary material under Code and data availability.

Erosional exhumation in T_c1D is driven by movement of material toward the model surface point (i.e., rock uplift). The surface point has a fixed location at 0 km depth in the model, which is equivalent to the local surface elevation on Earth. Depending on the defined surface temperature, this point could be at sea level or somewhere above or below. As the surface point is fixed in space, any movement of material by the defined velocity field in the model will produce erosion (or sedimentation) at a rate equal to the velocity. In other words, we assume any surface uplift (or subsidence) is perfectly balanced by erosion (or sedimentation). Movement of material toward (or away from) the surface in T_c1D is defined in various "erosion models". Examples include vertical motion at a constant velocity, multi-stage exhumation with step-function changes in the exhumation rate, vertical motion with an exponentially decaying rate, or convergent/extensional faulting where rates of motion vary above and below a defined fault depth. Details about each of the erosion models can be found in the online T_c1D documentation at https://tc1d.readthedocs.io/en/latest/erosion-models.html (Accessed on April 16, 2026) as well as in the supplementary material under Code and data availability.

All models presented here involve a significant amount of erosional exhumation because the calculated thermochronometer ages and closure temperatures in the models rely on the tracking particle reaching the surface at the end of the model run (hereafter called the final surface particle). Any scenarios involving insufficient exhumation will not capture the thermal history of the geological process under investigation. In these cases, the calculated cooling age will yield an unreset age roughly equivalent to the duration of the model, or a partially reset age. These cases are all clearly indicated as "partially/unreset" in the results. Such situations should also be clear in T_c1D thermal history plots, where ages for different chronometers are plotted on the thermal history at the time corresponding to their calculated age. A partially reset age, for example, could thus appear on a heating path. In this way, T_c1D can also be employed to explore minimum erosion magnitudes required to "capture" information about past geological processes using low-temperature thermochronology.

The complex effects of alpha damage accumulation on He retention in apatite and especially in zircon renders it impossible to accurately simulate He diffusion behavior in any models in which the final surface particle begins the simulation in a position of He and alpha damage accumulation (see also Whipp et al., 2022). Crystal damage is thought to anneal in a similar way, and under similar temperature conditions, to fission tracks (Flowers et al., 2009; Guenthner et al., 2013; Guenthner, 2021). Hence, most of the scenarios explored below involve a starting depth for which open system behavior is expected, and zircon or apatite should not have accumulated any alpha damage ($\sim 300°$ C). This is a recommended practice when using the T_c1D code.

Although we do not explore this in the presented results, it is also possible to vary the grain size and parent isotope concentrations for the AHe and ZHe systems in T_c1D. These values can be provided for single crystals in a T_c1D model by defining the relevant model parameters (e.g., `ap_rad` or `ap_uranium` for the effective spherical radius or uranium concentration in apatite). It is also possible to include multiple crystals of varying size and with variable parent isotope concentrations using an age data file, as described in the online documentation at https://tc1d.readthedocs.io/en/latest/age-data.html (Accessed on April 16, 2026). In addition, sensitivity to ranges of grain dimensions and parent isotope concentrations can be explored using the thermal history that is saved in the `csv` directory where T_c1D is run and importing that into $T_c$plotter (Whipp et al., 2022).

2.3 Modeled scenarios

Five common geological processes are explored with T_c1D. The first set of 12 models explores various styles of erosional exhumation (EE), followed by 6 sedimentary burial models (SB), 4 thrust faulting (TF) models, 4 extensional faulting (EF) models, and 4 lithospheric delamination models (DL) (Table 1, Fig. 2). The scenarios presented are not intended to be exhaustive, or tailored to fit a particular natural analogue, but rather are designed to explore the sensitivity of low temperature thermochronometers to the effects of heat transfer influenced by these various processes. The different geological scenarios primarily affect movement of material within the model, resulting in heat transfer by advection and displacement of a thermal history tracking particle. Each model has a thickness of 125 km and a final Moho depth of 35 km. More detailed descriptions of each scenario are given below and other common model parameters are summarized in Table 2.

2.3.1 Erosional exhumation (EE) models

The EE models explore the effect of a time-varying rate of erosional exhumation on predicted thermochronometer ages over a 50 Myr duration. In these models, the rate of erosional exhumation is either constant, has a step-function increase after 5 or 45 Myr, or decreases following an exponential function with different characteristic times for decay. The total amount of

Table 1. $\mathrm{T_c}$1D modelled scenarios

Model	VHP	Time intervals (Ma in the model framework)										
		$55-50$	$50-45$	$45-40$	$40-35$	$35-30$	$30-25$	$25-20$	$20-15$	$15-10$	$10-5$	$5-0$
EE1	2.0	–	Erode 10 km									
EE2	1.0	–	Erode 10 km									
EE3	1.0	–	Erode 5 km	Erode 5 km								
EE4	1.0	–	Erode 5 km									Erode 5 km
EE5	2.0	–	Erode 20 km									
EE6	1.0	–	Erode 20 km									
EE7	1.0	–	Erode 10 km	Erode 10 km								
EE8	1.0	–	Erode 10 km									Erode 10 km
EE9	2.0	–	Erode 10 km, exponentially decaying erosion with 2 Myr decay constant									
EE10	1.0	–	Erode 10 km, exponentially decaying erosion with 10 Myr decay constant									
EE11	1.0	–	Erode 10 km, exponentially decaying erosion with 50 Myr decay constant									
EE12	1.0	–	Erode 20 km, exponentially decaying erosion with 2 Myr decay constant									
SB1	2.0	–	Deposit 9 km		Erode 10 km							
SB2	1.0	–	Deposit 9 km		Erode 10 km							
SB3	2.0	–	Deposit 9 km				Erode 10 km					
SB4	1.0	–	Deposit 9 km				Erode 10 km					
SB5	2.0	–	D9 / Erode 10 km over 49 Myr									
SB6	1.0	–	D9 / Erode 10 km over 49 Myr									
TF1	1.0	Steady state	6.25 km HW uplift	Erode 8.75 km, (0.5 km above fault in HW)								
TF2	1.0	Steady state	6.25 km FW burial	Erode 8.75 km, (0.5 km below fault in FW)								
TF3	1.0	Steady state	12.5 km HW uplift	Erode 2.5 km, (0.5 km above fault in HW)								
TF4	1.0	Steady state	0.0 km FW burial	Erode 2.5 km, (0.5 km below fault in FW)								
EF1	1.0	Steady state	6.25 km HW burial	Erode 8.75 km, (0.5 km above fault in HW)								
EF2	1.0	Steady state	6.25 km FW uplift	Erode 8.75 km, (0.5 km below fault in FW)								
EF3	1.0	Steady state	0.0 km HW burial	Erode 2.5 km, (0.5 km above fault in HW)								
EF4	1.0	Steady state	12.5 km FW uplift	Erode 2.5 km, (0.5 km below fault in FW)								
DL1	1.0	Steady state	DL 15 km*	Erode 15 km								
DL2	1.0	Steady state	DL 15 km*	Erode 15 km, exponentially decaying erosion with 2 Myr decay constant								
DL3	1.0	Steady state	DL 15 km*	Erode 15 km, exponentially decaying erosion with 10 Myr decay constant								
DL4	1.0	Steady state	DL 15 km*	Erode 15 km, exponentially decaying erosion with 50 Myr decay constant								

All rates of erosion or deposition are constant over the interval unless otherwise stated. Scenarios have a 50 (EE and SB) or 55 (TF, EF, DL) Myr duration. TF, EF, and DL models include an initial 5 Myr of thermal steady state ($55-50$ Ma) before faulting/delamination. Acronyms and table symbols: VHP: volumetric heat production in $\mu\mathrm{W}\cdot\mathrm{m}^{-3}$; EE: erosional exhumation; SB: sedimentary burial; TF: thrust faulting; EF: extensional faulting; DL: delamination of the continental lithospheric mantle; D9: deposit 9 km in 1 Myr; *: delamination of the subcontinental lithospheric mantle and juxtaposition of asthenosphere against the base of the crust is performed instantaneously in the model at $t = 50$ Ma.

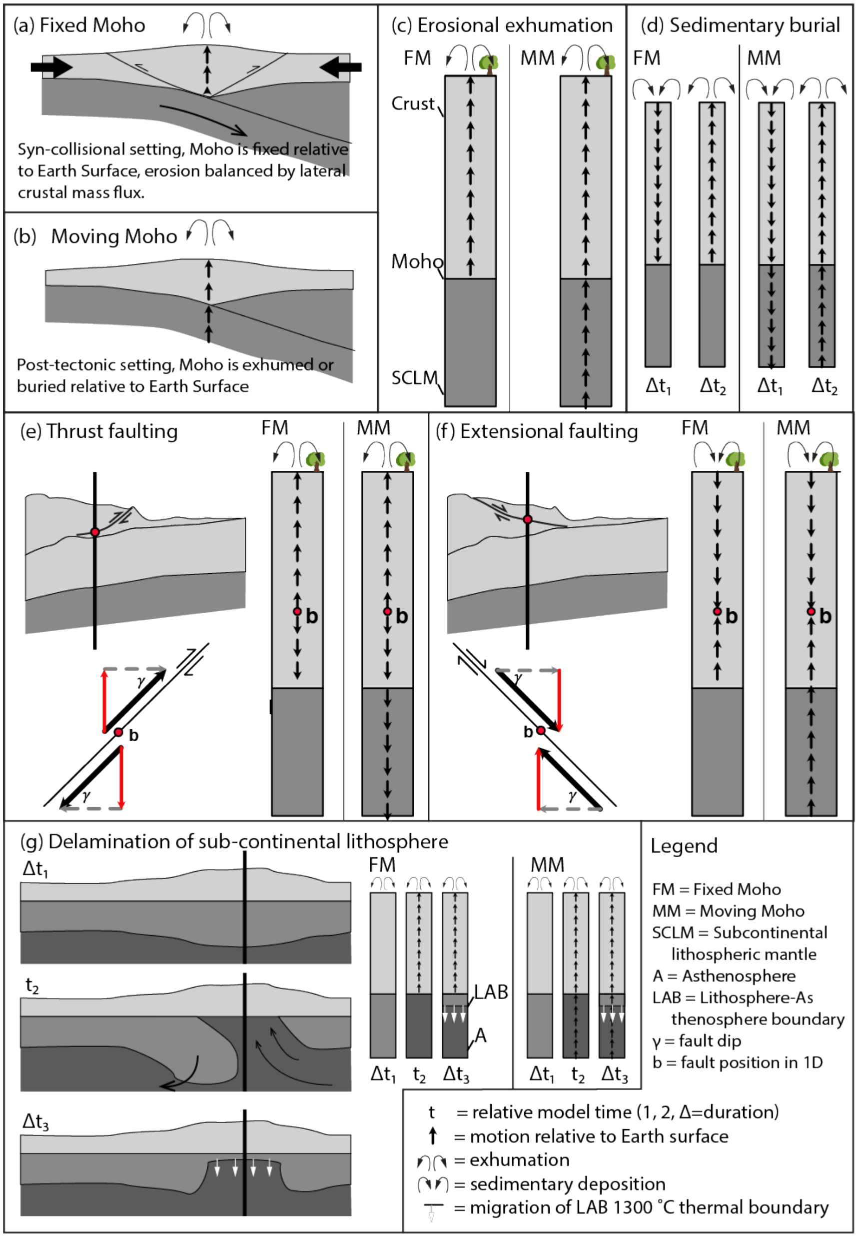

Figure 2. Schematic diagrams of 1D model types listed in Table 1, with the vertical black line depicted in all cross sections simulating the 1D position of the model. Each scenario is modeled with both a fixed (a) and moving (b) Moho, broadly analogous to syn- and post-tectonic settings as depicted in (a) and (b) and as denoted in (c)–(f) as FM and MM, respectively. Modeled scenarios include explorations of (c) erosional exhumation, (d) sedimentary burial, (e) thrust faulting, (f) extensional faulting and (g) delamination of the sub-continental lithospheric mantle.

Table 2. $\mathrm{T_c}$1D model parameters

Parameter	Value*	Unit
	General parameters	
Thickness	125	km
Spatial resolution	0.5	km
Duration	50 – 55	Myr
Time step, explicit	500	yr
Time step, implicit	5000	yr
Initial Moho depth	35 – 50	km
	Thermal parameters	
Surface temperature	0	°C
Basal temperature	1300	°C
Density†	2850, 3250, 3250	$\mathrm{kg \cdot m^{-3}}$
Heat capacity†	800, 1000, 1000	$\mathrm{J \cdot kg^{-1} K^{-1}}$
Thermal conductivity†	2.75, 2.5, 20.0	$\mathrm{W \cdot m^{-1} K^{-1}}$
Volumetric heat prod.†	1–2, 0, 0	$\mu\mathrm{W \cdot m^{-3}}$
	Thermochronometer parameters	
Grain radius‡	45, 60	μm
U concentration‡	10, 100	ppm
Th concentration‡	40, 40	ppm

* Varied parameters shown as ranges

† List order: Crust, mantle lithosphere, asthenosphere

‡ List order: Apatite, zircon

exhumation is either 10 or 20 km, and the constant-rate models produce this amount of exhumation linearly over 50 Myr. The step-function models have either 5 or 10 km of exhumation over the initial or final 5 Myr of the simulation, with the remaining 5 or 10 km of exhumation evenly distributed over the remainder of the simulation time. The exponential models produce 10 km of exhumation with characteristic decay times of 2, 10 or 50 Myr, as well as 20 km of exhumation with a characteristic decay time of 2 Myr. The volumetric radiogenic heat production in the crust is either average ($1\ \mu\mathrm{W \cdot m^{-3}}$) or high ($2\ \mu\mathrm{W \cdot m^{-3}}$) (Table 1; Fig. 2).

For each exhumation style, the EE models also consider two variations: one where the Moho depth shallows during exhumation and another where the Moho depth remains constant. The models for which the Moho shallows during exhumation (hereafter referred to as MM for moving Moho, see Fig. 2b) simulate erosional exhumation in a post-tectonic setting where the crust is thinned due to erosion driven by isostasy (e.g., type 3 of Wolf et al., 2022), which results in movement of the entire lithosphere toward the surface. Thus, these models have a velocity field that is constant across the entire model thickness. In contrast, models with a constant Moho depth (hereafter referred to as FM for fixed Moho, see Fig. 2a) represent a steady-state, syn-collisional setting in which erosional exhumation is balanced by a crustal mass flux via shortening and/or crustal flow at depth (e.g., type 2 of Wolf et al., 2022). In this case, the erosional exhumation velocity is only applied to the model crust and the velocity below the crust is zero. In both cases, the Moho depth at the end of the simulation is 35 km. It is illustrative to compare both scenarios (FM and MM) because the evolution of the Moho depth is not often considered when modeling low-T thermochronological data, and yet it exerts an influence on the thermal structure of the crust, and hence on thermochronometer ages. We have chosen to present scenarios in which the final Moho depth is identical between the two runs, rather than having equal starting Moho depths, because it is more representative of the challenge facing the geologist–a myriad of different possible trajectories through temperature-depth-time (T-d-t) space could produce the present day thermal and geological structure of the crust and pattern of thermochronological data.

2.3.2 Sedimentary burial (SB) models

The SB models are somewhat similar to the EE models but involve a phase of sedimentary deposition at the start of the model prior to erosional exhumation. In each case, 9 km of sediment is initially deposited over 1, 10, or 20 Myr resulting in variable sedimentation rates referred to as high, intermediate and low. Following deposition, 10 km of material is eroded (9 km of sediment and 1 km of basement) over the remainder of the 50 Myr model duration. In contrast to the EE models, however, only moving Moho cases are considered and thus the sedimentation and erosion velocities are applied across the full model thickness. In addition, model variants include average ($1\ \mu\mathrm{W}\cdot\mathrm{m}^{-3}$) and high ($2\ \mu\mathrm{W}\cdot\mathrm{m}^{-3}$) crustal radiogenic heat production, similar to the EE models (Table 1; Fig. 2).

2.3.3 Thrust faulting (TF) models

The TF models are designed to simulate the contrasting exhumation histories experienced by rocks in the hanging wall and footwall of thrust faults. Crustal-scale faults commonly show contrasting thermochronometer age patterns between hanging wall (HW) and footwall (FW) samples, particularly for thrust and normal dip-slip fault types in which rocks from different structural levels may be juxtaposed (e.g., Stockli, 2005). Classical 1D thermal models of thrust faulting, first presented by Oxburgh and Turcotte (1974), have typically simulated the thermal effects of thrust activity via instantaneous stacking of the crustal thrust nappes. This creates an initial sharp step in temperature-depth space that duplicates the geothermal gradient in the upper crust, subsequent thermal relaxation in which the HW is cooled and the FW is heated by their juxtaposition across the fault, and an eventual re-establishment of the conductive geothermal gradient across the thickened crust. Associated crustal thickening would likely promote erosional exhumation due to isostatic uplift, particularly focused in the HW. More complex 2D thrust fault and fold-and-thrust belt models have compared low temperature thermochronology data against forward modeled fold-and-thrust belt evolutions involving one or multiple active structures, predicting along-strike patterns in thermal history and thermochronometer ages between the footwall and hanging wall (e.g., U-shaped patterns; Lock and Willett, 2008), and across fold belts (e.g., McQuarrie and Ehlers, 2015; McQuarrie et al., 2017).

The TF models target a model design of intermediate complexity, using a single fault system that can be activated for a desired duration, specified slip rate, and fault dip angle, and simultaneous with surface erosion (or deposition if subsidence occurs). Faulting scenarios are explored in T_c1D using a framework in which the fault is initially positioned at a specified depth b, with a prescribed dip angle γ, and a slip rate of v (Fig. 2e). Movement across the fault is divided between the HW and FW via a partitioning factor λ, such that $\lambda = 1$ represents a fixed HW and $\lambda = 0$ represents a fixed FW. The corresponding vertical (1D) components of velocity due to fault slip in the footwall, $v_{z,\mathrm{fw}}$, and hanging wall, $v_{z,\mathrm{hw}}$, are:

$$v_{z,\mathrm{fw}} = \lambda v \sin\gamma \tag{1}$$

$$v_{z,\mathrm{hw}} = -(1-\lambda) v \sin\gamma \tag{2}$$

In TF scenarios, the FW is advected downwards and the HW is advected upwards during faulting (Fig. 2e). Frictional heating along the fault surface is ignored. As the horizontal component of motion and heat transfer is also ignored, the exercise of comparing contrasting thermal histories in selected HW and FW positions effectively requires two different 1D starting columns that converge when the total desired fault slip is completed (see Fig. A1). In such cases, the tracking particles in the HW and FW of two different models reach the same depth at the end of faulting and are subsequently exhumed by the same amount to the surface over the model duration. The TF models begin with a 5 Myr period with no fault movement or exhumation followed by a 5 Myr period of thrust fault activity on a fault with a slip rate of $v = 5$ km/Myr and dip angle of $\gamma = 30°$. During thrust faulting, any surface uplift or subsidence is balanced by erosion or deposition, respectively, such that the surface elevation does not change. Partitioning factors of $\lambda = 0.5$ and $\lambda = 0$ are used, with initial fault depths of $b = 15.5$ and 2 km for tracking particles located 500 m above and below the fault in the HW and FW, respectively. The difference in initial fault depth relates to how fault motion is defined. Final surface particles in the hanging wall will move upwards during fault motion, while particles in the footwall will move downwards. In both cases, the reference frame maintains a constant distance above or below the fault, resulting in the fault following the movement of the tracking particle (Fig. A1). The final stage is continued erosional exhumation of the tracking particle to the surface over the remaining 45 Myr of the simulation. Thus, all TF models have a duration of 55 Myr, over which 15 km of exhumation occurs. Both FM and MM kinematics are used, but only the average crustal radiogenic heat production value is considered (1 $\mu\mathrm{W \cdot m^{-3}}$) (Table 1; Fig. 2).

2.3.4 Extensional fault (EF) models

The EF models are effectively identical to the TF models described above, with the only significant difference being a reversed fault slip direction. The models feature a 5 Myr period of no motion or erosion (steady state), 5 Myr of faulting, and 45 Myr of erosional exhumation following faulting, totaling 15 km of exhumation over the 55 Myr model duration. During extensional faulting, any surface uplift or subsidence is balanced by erosion or deposition, respectively, such that the surface elevation does not change. Similar to the TF models, fault motion advects model particles in the HW and FW of paired models to the same depths before equal amounts of exhumation transport them to the surface for the final 45 Myr of the model run. As before, particles located 500 m above and below the fault are tracked, which requires initial fault depths of $b = 14.5$ and 3 km for tracking particles in the FW and HW, respectively. FM and MM scenarios are considered and an average crustal radiogenic heat production (1 $\mu\mathrm{W \cdot m^{-3}}$) is used.

2.3.5 Lithospheric delamination (DL) models

The DL models simulate the thermal and thermochronometer age effects of instantaneous removal of the mantle lithosphere, its replacement by asthenospheric material, and thermal relaxation during subsequent erosional exhumation. Lithospheric delamination and dripping are density-driven processes in which the sub-continental lithospheric mantle (and possibly lower crust) founders, detaches, and sinks into the asthenosphere, juxtaposing hot asthenosphere against the base of the remaining crust (Ducea, 2011; Göğüş and Ueda, 2018; McMillan and Schoenbohm, 2023). Signatures of past delamination and drip are thought to include a shift in magmatism towards more deeply-sourced, mafic magmatism (Kay and Mahlburg Kay, 1993; Drew et al., 2009) and rapid surface uplift during the foundering or detachment stages (Garzione et al., 2006, 2008), sometimes preceded by burial/deposition and heating during the foundering stage (McMillan and Schoenbohm, 2023). For more recent lithospheric removal events, the lithospheric mantle may be imaged as thin or non-existent (e.g., Bezada et al., 2014). In some cases, the delaminated slab may still be imageable in the mantle (e.g., Zandt et al., 2004; Bao et al., 2014; Bezada et al., 2014).

Because delamination produces both a thermal and surface process response due to uplift or subsidence/deposition, its impact on the upper crust may be recorded in the low-temperature thermochronology record. Hence the timing and nature of lithospheric delamination have been studied using low-temperature thermochronometry, and/or interpreted inflections in exhumation rate based upon low-temperature thermochronometer data have been linked to lithospheric delamination as a causative process (e.g., Dai et al., 2013; Bao et al., 2014; Bidgoli et al., 2015; Fraser et al., 2021).

The DL models simulate removal of the continental lithospheric mantle and juxtaposition of the asthenosphere against the base of the crust, followed by exhumation over the remainder of the model duration. Since delamination and drip involve both top-down surface processes and bottom-up heat conduction/advection, it is useful to examine the timescales and interactions of these erosional and heat-transfer processes. The DL models feature 5 Myr at the start with no exhumation or delamination, instantaneous delamination of the entire mantle lithosphere after 5 Myr, and 15 km of erosional exhumation over the remaining 50 Myr of the model time. Temperatures in the asthenospheric material are defined by a mantle adiabatic temperature gradient (Turcotte and Schubert, 2014) initially for the entire mantle at 5 Myr and the mantle lithosphere regrows by conductive cooling (Fig. 2). Because we have not attempted to link a surface process model to the 1D models in $\mathrm{T_c}$1D, we explore delamination under various exhumation scenarios, including a constant rate of erosional exhumation following delaminationand exhumation with an exponential function with varying characteristic decay times of 2, 10, and 50 Myr. Both FM and MM scenarios are considered with an initial Moho depth of 50 km for the MM scenarios, such that the Moho ends up at 35 km depth for both models. Only an average crustal radiogenic heat production value is considered ($1\ \mu\mathrm{W} \cdot \mathrm{m}^{-3}$).

3 Results

Here we present an overview of predicted thermal histories and thermochronometer ages from ~ 30 model designs. Many of the models include FM and MM variants, as well as cases where the crustal radiogenic heat production varies. To aid in this discussion, we illustrate the impact model factors that affect temperatures in the crust using two dimensionless numbers: the Péclet number (Pe) and dimensionless heat production (f; see Appendix A of Batt and Braun, 1997). The Péclet number measures the relative contribution of heat transfer via advection to conductive heat transfer, and is defined as

$$\mathrm{Pe} = \frac{vL}{\kappa}, \tag{3}$$

where v is the advection velocity, L is the thickness of the advected layer, and κ is the thermal diffusivity ($\kappa = \frac{k}{\rho c_p}$, where k is thermal conductivity, ρ is density, and c_p is specific heat capacity). Pe values greater than one indicate advection is the dominant heat transfer process, while values close to zero for Pe ~~inticate~~ indicate heat conduction is dominant and advection has little effect on the model temperatures. The dimensionless heat production is defined as

$$f = \frac{HL}{2kT_\mathrm{L}}, \tag{4}$$

where H is volumetric heat production and T_L is the temperature at depth where temperature is assumed to remain constant. The dimensionless heat production operates similar to Pe, with values close to zero indicating little effect of heat production on the thermal field, and values greater than one indicating a strong contribution of heat production to model temperatures.

3.1 Erosional exhumation-type thermal histories

Twelve EE scenarios were explored, in which various magnitudes of exhumation and volumetric heat production, and different exhumation histories were applied over the 50 Myr of model run time (Fig. 2c; Table 1).

EE1, in which 10 km of material was removed via constant exhumation at a rate of 0.2 km/Myr, shows FM and MM thermal histories for the final surface particle that are slightly concave upwards, reflecting the modest rate of exhumation. Tracked particles start cooling from $\sim 290°$ C and $\sim 320°$ C for the FM and MM model variants, respectively, reaching 0° C at 0 Ma, or the model present (Fig. 3a). The different initial temperature at 10 km depth for the FM history versus the MM history relates to the differing initial Moho depths (35 km vs. 45 km, respectively), and initial temperatures at the Moho ($\sim 700°$ C and $\sim 900°$ C, respectively; see also supplementary plots under Code and data availability), which together result in different geothermal gradients and crustal temperature evolutions for the two scenarios. The Pe values also reflect the moderate rate of exhumation, with a constant value of ~ 0.2 for the FM model and ~ 0.9 for the MM model, indicating only a limited effect of exhumation on the crustal temperatures. The difference in Pe values results from application of the advection velocity to only the crust in the FM model, while the entire lithosphere is advected in the MM model. Both final surface particle starting temperatures are likely hot enough to produce open system/annealing behavior in all four low-temperature thermochronometers. The thermochronometer closure/annealing temperatures between the FM and MM scenarios are nearly identical, but the ages differ between the two scenarios because of the different thermal histories. The ZFT age for the MM scenario is ~ 7 Myr younger than for the FM scenario (the ages differ by ~ 20 %), with smaller differences in cooling age for the lower temperature thermochronometers as the two thermal histories converge towards 0 Ma at the surface.

EE2 is nearly identical to EE1, with 10 km of material being removed via constant exhumation, except the volumetric heat production of the (entire) crust is lowered to $1\ \mu\mathrm{W} \cdot \mathrm{m}^{-3}$. The thermal history for the final surface particle in EE2 is similar to EE1, but with much cooler starting temperatures of $\sim 200°$ C for the FM and MM scenarios, corresponding to an initial geothermal gradient for the upper 10 km of crust of only about 20° C/km. ~~These lower temperatures are also apparent These~~

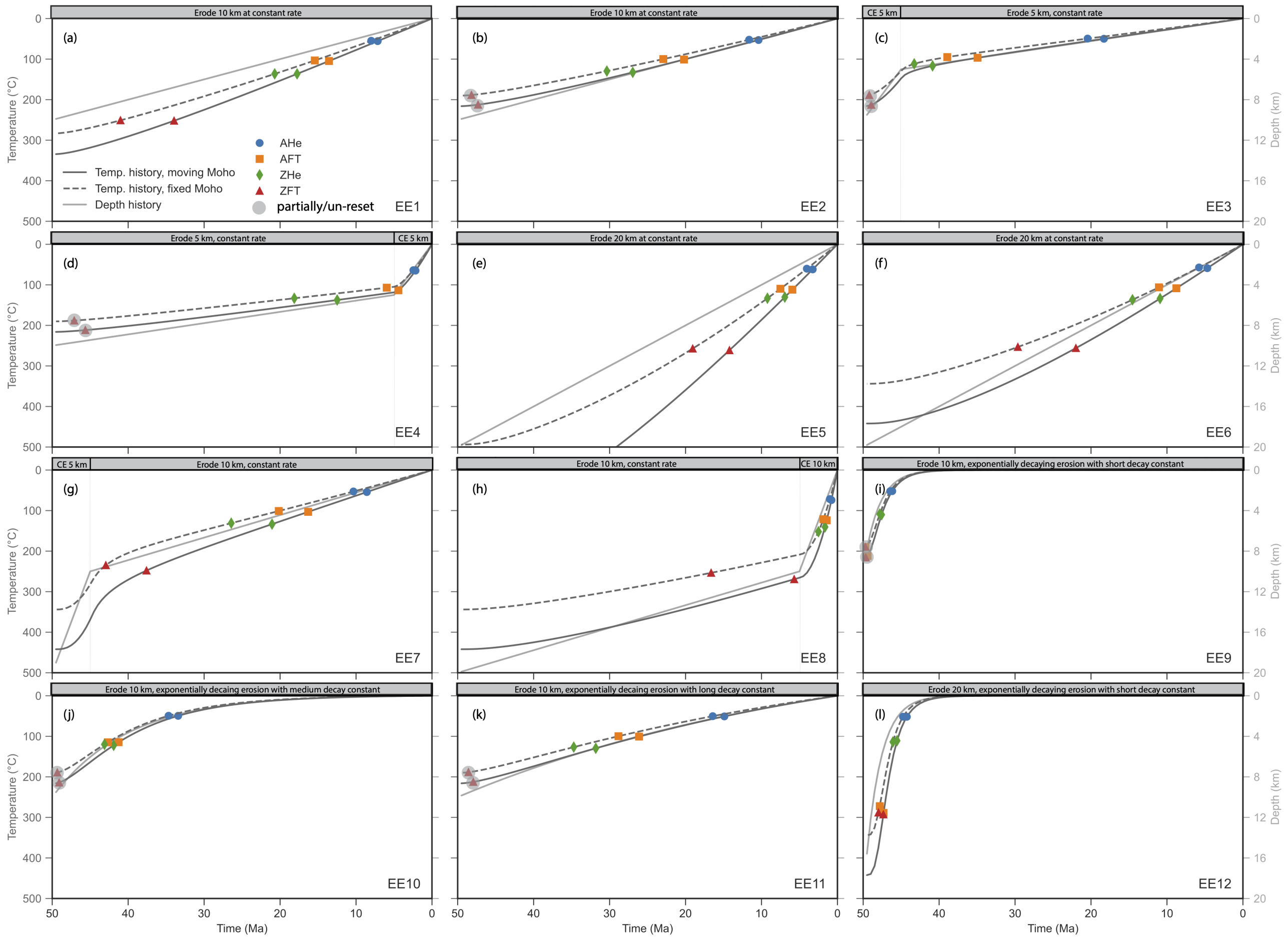

Figure 3. Erosional exhumation models, for which volumetric heat production is set at "average", or 1 $\mu\mathrm{W}\cdot\mathrm{m}^{-3}$, unless otherwise specified: (a) model EE1, in which 10 km is eroded at a constant rate over 50 Myr, and volumetric heat production is set at "high", or 2 $\mu\mathrm{W}\cdot\mathrm{m}^{-3}$; (b) model EE2, same erosion as (a) but average volumetric heat production; (c) model EE3, in which 5 km is eroded in the first 5 Myr and an additional 5 km is eroded over 45 Myr; (d) model EE4, in which 5 km is eroded in the first 45 Myr, and an additional 5 km is eroded in the final 5 Myr; (e) model EE5, in which 20 km is eroded at a constant rate over 50 Myr, and volumetric heat production is "high"; (f) model EE6, same erosion as (e) but average volumetric heat production; (g) model EE7, in which 10 km is eroded in the first 5 Myr and an additional 10 km is eroded in the final 5 Myr; (h) model EE8, in which 10 km is eroded in the first 45 Myr, and an additional 10 km is eroded in the final 5 Myr; (i) model EE9, in which 10 km is eroded over 50 Myr at an exponentially-decaying rate using a short decay constant, and volumetric heat production is set to high; (j) model EE10, in which 10 km is eroded over 50 Myr at an exponentially-decaying rate using a medium decay constant; (k) model EE11, in which 10 km is eroded over 50 Myr at an exponentially-decaying rate using a long decay constant, and finally (l) model EE12, in which 20 km is eroded over 50 Myr at an exponentially-decaying rate using a short decay constant. Parameters varied in each model are also described in Table 1.

~~lower initial temperatures~~ Due to lower initial temperatures that are within or cooler than the partial annealing temperature range for ZFT, ~~so~~ the ZFT age is ignored here and in all subsequent models for which total exhumation is only 10 km. The thermal history trajectories for the FM and MM scenarios show less difference than in EE1. ~~This is a result of having~~ Despite contrasts in starting Moho temperature similar to the EE1 models of $\sim 500°$ C and $\sim 700°$ C, respectively, there is less difference in ~~their~~ the FM and MM geotherms at shallow depths due to the lower radiogenic heat production~~value, despite similarly large contrasts in starting Moho temperature of $\sim 500°$ C and $\sim 700°$ C, respectively. The cooling ages~~ . In these models, the dimensionless heat production f is ~ 0.7, which is half its value in the EE1 models. However, as the thickness and rates of the exhumed layers have not changed compared to the EE1 models, the Pe values for the EE2 models are identical to those in EE1. The result is cooling ages that differ by 35 % on average between EE1 and EE2 (e.g., AFT and ZHe ages are respectively ~ 7 and ~ 9 Myr older in EE2), largely as a result of the cooler initial temperature of the final surface particles.

EE3 and EE4 are two-stage linear exhumation models that incorporate the same total amount of exhumation and volumetric heat production as in EE2, but either an initial 5 Myr period of rapid exhumation at 1 km/Myr followed by slower exhumation at ~ 0.1 km/Myr over the remaining 45 Myr (EE3), or slower exhumation during the initial 45 Myr and a final 5 Myr period of rapid exhumation (EE4). These exhumation histories produce average Pe values of ~ 0.2 and ~ 0.9 for the FM and MM models, respectively, that are similar to the EE1 and EE2 models. However, the difference in exhumation rates over time yields maximum Pe values reach ~ 0.9 for the FM variants and ~ 4.5 for the MM variants, indicating efficient advective heat transfer during more rapid exhumation. In EE3, the early, rapid exhumation results in significantly older ages compared to EE2, while in EE4 the late rapid exhumation results in significantly younger low-temperature thermochronometer ages. Note that despite the common erosion rate while traversing the effective closure temperatures of the ZHe and AFT systems for these two models, the lag between the two systems is much shorter for EE3 (~ 5 Myr) than for EE4 (~ 10 Myr), due to the immediately preceding period of rapid erosion and cooling.

EE5 and EE6 represent fairly extreme erosional models in which 20 km of crust is removed in 50 Myr, corresponding to a long-lived constant erosion rate of 0.4 km/Myr. The difference in Moho depth in the MM scenario thus also differs by 20 km, resulting in an unrealistically hot starting Moho temperature of $\sim 1200°$ C for EE5, in which the crust has a high heat production value ($2\ \mu\mathrm{W}\cdot\mathrm{m}^{-3}$), and $> 850°$ C for EE6, in which the crust has an average heat production value ($1\ \mu\mathrm{W}\cdot\mathrm{m}^{-3}$). Though these are high Moho temperatures, the models are nevertheless instructive in accentuating the heat conduction effects observed in EE1 and EE2.

The cooling paths in EE5 and EE6 show more curvature than in EE1 and EE2, despite the constant erosion rate, as the final surface particle begins closer to the Moho and farther from the surface. The cooling rate initially is low following the onset of exhumation (and heat advection) before beginning to increase and produce a curved cooling trajectory. This curvature results from curvature in the geotherm (changes in the geothermal gradient with depth) as the result of more efficient advective heat transfer. In these models, the Pe values are ~ 0.4 for the FM variants and ~ 1.8 for the MM variants, double those for the EE1 and EE2 models. As the tracking particle nears the surface, the cooling path becomes more linear through the upper 10 km of exhumation, similar to EE1 and EE2. In these and all EE models, the shape of the thermal and depth histories match most closely in the uppermost crust, below ~ 10 km depth and $\sim 250°$ C and mainly show deviations at higher temperatures and deeper crustal depths. The ages for the four thermochronometers are clustered most closely in EE5, and particularly in the EE5 MM scenario, compared to any of the other scenarios explored thus far, spanning ca. 11 Myr. This reflects the high geothermal gradient from the high, sustained exhumation rate and high heat production for EE5. ZHe and AFT ages are particularly close and would be indistinguishable for typical reported errors of those methods.

Similar to EE3 and EE4, scenarios EE7 and EE8 explore two-stage linear exhumation models, but in which half of the 20 km total exhumation occurs in either the first 5 million years of run time (EE7) or the last 5 million years of run time (EE8) at a rate of 2 km/Myr, and erosion throughout the remainder of each model occurring at ~ 0.2 km/Myr. In both FM and MM versions of EE7, the period of rapid exhumation at the model start shows a significant geometric deviation between the linear depth history and an S-shaped thermal history. The initial period of rapid exhumation (maximum Pe values of ~ 1.8 and ~ 9.0 for the FM and MM variants, respectively) advects heat upwards with limited cooling and the thermal adjustment to the slower cooling rate then lags behind the decrease in the exhumation rate. Thus, cooling ages may similarly lag behind the change in exhumation rate. However, since all thermochronometers close on the slow-exhumation segment of the depth history path, this deviation does not impact cooling ages in EE7, and the cooling age patterns in the MM and FM models are relatively similar to EE1. In EE8, there is a similar lag in the thermal history compared to the depth history during the rapid exhumation phase, here occurring in the last 5 Myr of the model, although the deviation is much smaller than in EE7 due to being closer to the model surface, with limited space to exhume without cooling. In this model, the difference in depth history for the FM and MM scenarios results in a ZFT age that is ~ 11 Myr older (an increase of ~ 190 %) in the FM scenario, despite its lower calculated effective closure temperature. Otherwise, rapid cooling through the upper crust shows a relatively close alignment between thermal and depth histories, and between the FM and MM scenarios.

In scenarios EE9–EE12, exponentially decaying exhumation rates are explored, with short (EE9), medium (EE10), and long (EE11) characteristic decay times of 2, 10, and 50 Myr, respectively. Each model involves erosional removal of 10 km of crust, as well as an exhumation scenario with 20 km of erosional exhumation (EE12) and a 2 Myr characteristic time. The low decay scenario, EE11, has a gently-curving, ~~near linear~~ near-linear cooling path, making it quite similar to EE2. The average Pe values (~ 0.2 (FM) and ~ 0.9 (MM)) for this case are identical to EE2, and the maximum Pe values only reach ~ 0.3 (FM) and ~ 1.4 (MM). However, the medium and high exponent scenarios (EE9, EE10, EE12) show FM and MM thermal histories that quite closely follow the depth history, in contrast to most of the linear exhumation scenarios described above. In EE10, there is a brief period of limited cooling at the start of the simulation, after which the cooling histories follow the depth history as the exhumation rate decreases. In EE9, the cooling and depth histories are nearly indistinguishable. Although the exhumation rate decays over the same time in EE9 and EE12, the starting depth and rate of exhumation is twice as high in EE12, producing an initial period of limited cooling (where advection dominates conductive cooling) before tracking the shape of the depth history. This ~~initial rapid cooling~~ efficient advection is reflected in maximum Pe values for EE9, EE10, and EE12 of 4.4 – 42.6 for the MM variants, and produces a small lag between the thermal and depth histories. In all of the intermediate and rapidly decaying exponential exhumation rate models (EE9, EE10, and EE12), the thermochronometer ages would be indistinguishable between the FM and MM scenarios within typical reported errors. However, the two high-exponent scenarios (EE9, EE12) both predict an inverted relationship of ZHe ages younger than AFT ages, while the medium exponent scenario in EE10 results in ZHe

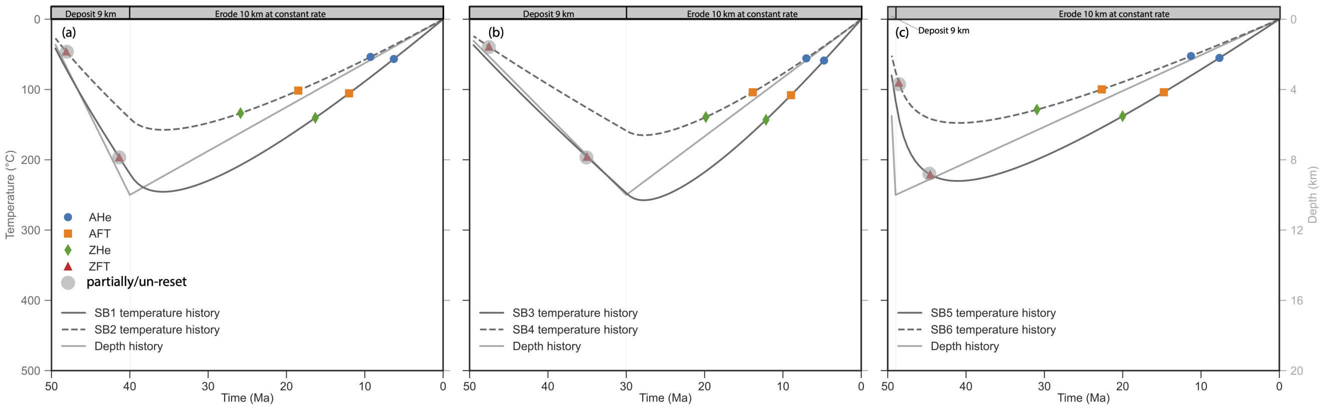

Figure 4. Sedimentary burial models: (a) models SB1 and SB2, with high and average volumetric heat production, respectively, in which 9 km is deposited at surface over 10 Myr, followed by 10 km of erosion at a constant rate over 40 Myr ; (b) SB3 and SB4, with high and average volumetric heat production, respectively, in which 9 km is deposited at surface over 20 Myr, followed by 10 km of erosion at a constant rate over 30 Myr ; (c) SB5 and SB6, with high and average volumetric heat production, respectively, in which 9 km is deposited at surface over 1 Myr, followed by 10 km of erosion at a constant rate over 49 Myr . Parameters varied in each model are also described in Table 1.

ages almost equal to AFT ages, matching the pattern reported in Whipp et al. (2022) for low eU-rapid and low eU-intermediate linear cooling rates (see their Fig. 5b).

3.2 Sedimentary burial-type thermal histories

Models SB1–SB6 explore the influence of different rates of sedimentary burial and different volumetric heat production values during burial and exhumation. SB1 and SB2 have intermediate sedimentary burial rates of 0.9 km/Myr for the first 10 Myr followed by 40 Myr of exhumation at a rate of 0.25 km/Myr (average Pe values: ~ 1.7; maximum Pe values: ~ 4.1), and crustal radiogenic heat production values of 2 and 1 $\mu\mathrm{W} \cdot \mathrm{m}^{-3}$, respectively (Fig. 4a). The peak temperature experienced by the final surface particle in the basement beneath the added sedimentary package reaches $\sim 240°$ C in SB1 compared to $\sim 160°$ C in SB2. This difference is the result of dimensionless heat production values in SB2 of ~ 0.7, which are half those in SB1. In both models, the basement rocks reach peak temperatures slightly later than their peak burial depths, lagging by about $4-5$ Myr. Cooling ages in the cooler SB2 scenario are significantly older compared to the SB1 scenario (e.g., the ZHe ages differ by ~ 46 % or ~ 10 Myr older) due to the higher peak temperatures associated with higher rates of radiogenic heat production, but the effective closure temperatures are similar. The lag in age between ZHe and AHe is ~ 10 Myr in SB1, compared to ~ 16 Myr in SB2. As with the above EE models, the ZFT thermochronometer does not reach a temperature sufficient for annealing in any of the SB models and is ignored here.

SB3 and SB4 involve the same amount of sedimentary burial and exhumation as SB1 and SB2, except the burial rate is slower (0.45 km/Myr) over 20 Myr and exhumation is more rapid at a rate of ~ 0.33 km/Myr over the remaining 30 Myr (Fig. 4b). As before, SB3 is the high volumetric heat production scenario, with SB4 being the average (values of 2 and 1

$\mu\mathrm{W}\cdot\mathrm{m}^{-3}$, respectively). Peak temperatures reached for the final surface particle (corresponding to basement rock originally lying 1 km beneath the eroded basin) in SB3 are $\sim 250°$ C and in SB4 are $\sim 175°$ C, slightly higher than for SB1 and SB2, respectively, due to the slower rate of sedimentation and less cooling from thermal advection (maximum Pe values only ~ 2.0). Peak temperature conditions in both scenarios also have a shorter lag following the peak in burial depth, relative to SB1 and SB2, of only 2–3 Myr. This is due to less disturbance of the conductive geotherms from sedimentation at a slower rate. Because of the difference in peak temperature, cooling ages in SB4 are older than in SB3, for example ~ 8 Myr older for the ZHe thermochronometer. The difference in age between ZHe and AHe is ~ 7 Myr in SB3, and ~ 13 Myr in SB4.

The final two scenarios, SB5 and SB6, represent extreme scenarios, with a very high sedimentation rate of 9 km/Myr for 1 Myr followed by slow exhumation at ~ 0.2 km/Myr for the remaining 49 Myr (Fig. 4c). SB5, with high volumetric heat production (2 $\mu\mathrm{W}\cdot\mathrm{m}^{-3}$), reaches a peak temperature for the final surface particle of $\sim 220°$ C, while SB6, the average heat production scenario (1 $\mu\mathrm{W}\cdot\mathrm{m}^{-3}$), reaches a peak temperature of only $\sim 140°$ C, the lowest value among the SB model set. These models also show the longest lag of peak temperature following peak burial depth, at about 8 Myr. Here the rate lag is due to the larger perturbation of the conductive geotherm by the extremely rapid rate of sedimentary burial (maximum Pe values up to ~ 40.1). Cooling ages in SB6 are ~ 11 Myr older (ZHe) than in SB5, and the difference in age between ZHe and AHe is ~ 12 Myr in SB5 compared to ~ 19 Myr in SB6.

3.3 Thrust faulting-type thermal histories

Models TF1–TF4 explore the effects of thrust faulting on final surface particles in the hanging wall and footwall of a thrust fault (Fig. 5). The fault slip rate (5 km/Myr) and dip angle (30°) are the same in all models, and FM and MM variants are presented. In TF1 and TF2, fault motion is equally partitioned between FW and HW and as explained in Sect. 2.3.3, the initial fault depth b varies for hanging wall and footwall particle, with $b = 15.5$ km for TF1 and $b = 2$ km for TF2. In TF1, the HW thermal path for both MM and FM conditions shows a continuous cooling history, with accelerated cooling and exhumation during fault slip, a reduction in cooling immediately after fault motion ends, and a gradual increase in the rate of cooling as the final surface particle is exhumed. The FW thermal histories for this scenario, shown in TF2, show heating during faulting that slightly extends after faulting ceases, delaying significant cooling by around 10 Myr after fault cessation in both FM and MM results. Unfortunately, calculation of Pe numbers for this model type is not yet supported in $\mathrm{T_c1D}$. Since the fault position is at a deeper structural level, most of the lower temperature thermochronometers in TF1 and TF2 show similar cooling ages that are strongly influenced by post-faulting exhumation rather than the faulting stage. For instance, the ZHe ages for the MM scenarios in TF1 and TF2 differ only by ~ 4 Myr, which is the largest difference for AHe, AFT, and ZHe. However, the ZFT ages in model TF1 reflect cooling during fault activity, most clearly for the MM scenario. In this case, the ZFT age in the hanging wall is ~ 7 Myr younger than the equivalent age in the footwall, which is unreset.

In scenarios TF3 (HW) and TF4 (FW), the footwall remains fixed with respect to b (Fig. 5c), and all slip is partitioned into hanging wall motion, doubling its rate of motion toward the surface compared to TF1. The thermal history for the HW in this scenario correspondingly shows a more rapid cooling rate during fault slip than for TF1, followed by slower cooling to reach the surface at the end of the model run time than for TF1. As the final surface particle is exhumed closer to the surface during

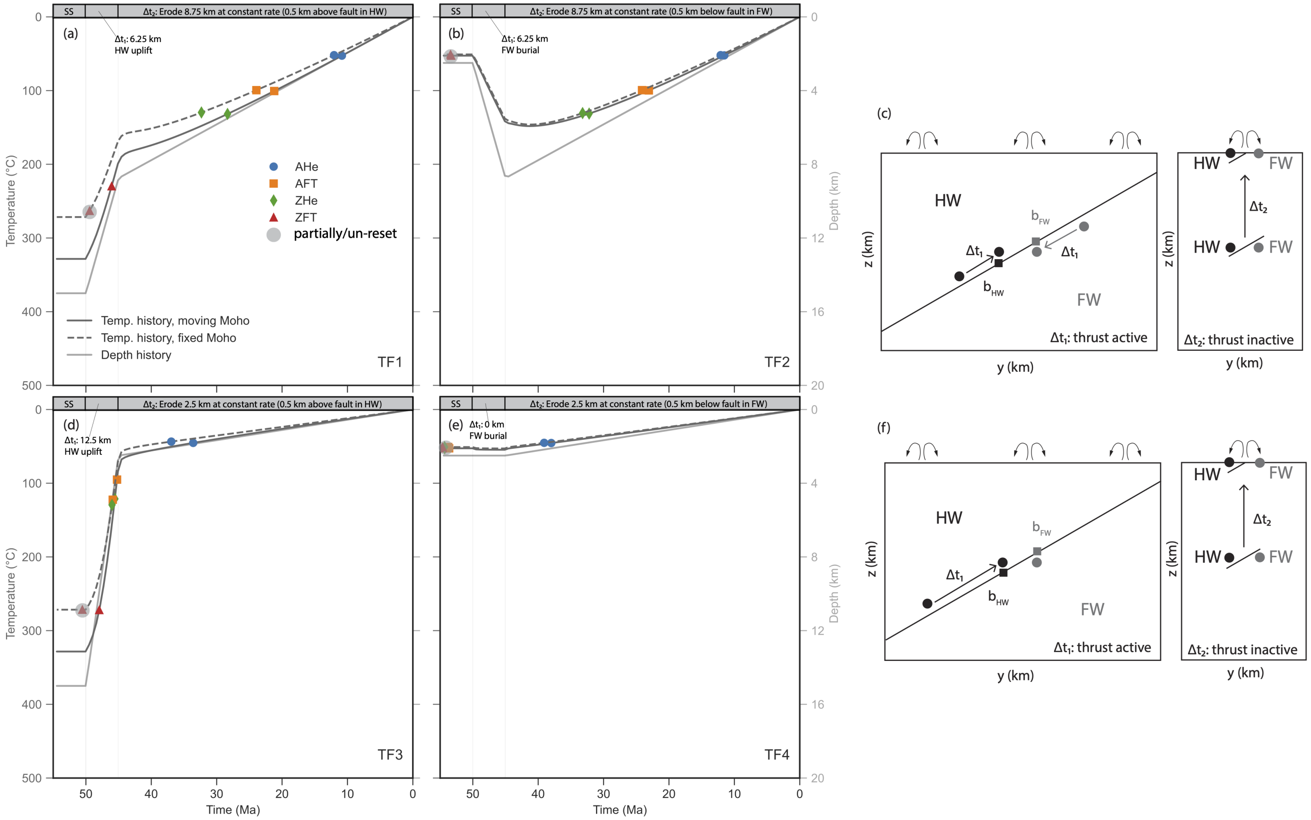

Figure 5. Thrust fault models. (a) and (b) show models TF1 and TF2, which are hanging wall and footwall thermal and depth histories, respectively, simulating the thrust fault displacement scenario described in (c) and Table 1: final surface particle paths for particles that are 500 m above the fault in the hanging wall and 500 m below the fault in the footwall, respectively, of a thrust fault dipping 30°, that was active over 5 Myr during 50–45 Ma with a partitioning factor of $\lambda = 0.5$ and then exhumed from 8.75 km to the surface. (d) and (e) show models TF3 and TF4, which are hanging wall and footwall thermal and depth histories, respectively, for the fault displacement scenario described in (f) and Table 1: same as TF1 and TF2 but with a fixed footwall ($\lambda = 0$) and exhumation from 2.5 km depth to the surface. Parameters varied in each model are also described in Table 1.

faulting than in TF1, the post-faulting cooling history is more linear compared to the concave upward cooling history in TF1 (Fig. 5a, c). The footwall is held in a fixed position during faulting and then exhumes once faulting has ceased. In this instance, FW heating caused by juxtaposition of the hotter HW is negligible and has no impact on the predicted thermochronometer ages. However, in contrast to TF1, most thermochronometer ages are controlled by fault-related uplift and erosional exhumation, nicely documenting the timing of fault slip in the HW. For example, the AFT, ZHe, and ZFT ages are all $\sim 45-50$ Ma in TF3. In contrast, the AFT, ZHe, and ZFT ages in TF4 are not reset. However, AHe ages are reset in both TF3 and TF4, reflecting post-faulting exhumation and with similar ages ($\sim 34-39$ Ma).

3.4 Extensional faulting-type thermal histories

The extensional faulting (EF) models use the same approach as for the TF scenarios, but with a reversed slip direction. Thus, the two different extensional faulting scenarios have a slip rate of 5 km/Myr during 50–45 Ma after an initial 5 Myr of steady state, producing equal end-of-slip fault depths in the upper crust for the HW and FW model variants (8.75 km for EF1 and EF2 and 2.5 km for EF3 and EF4). The final model stage comprises exhumation to the surface at the end of the model (Fig. 5; Table 1). The first set of models (EF1–EF2) use a partitioning factor of 0.5, while for the second set (EF3–EF4) the HW is fixed during faulting ($\lambda = 1$). For both scenarios, we examined a final surface particle situated 500 m above the fault in the HW (EF1, EF3), and a final surface particle situated 500 m below the fault in the FW (EF2, EF4). As above, calculation of Pe numbers for this model type is not yet supported in T_c1D.

In EF1 and EF2, the HW is buried from 2.5 km to 8.75 km during fault slip, while the FW block is continuously exhumed from 15 km to 8.75 km during fault slip, and the final surface particle in both scenarios is exhumed at a slower rate to the surface by the end of the model. Here, heating of the HW due to burial and subsequent cooling during exhumation closely follows the depth history of the particle in EF2. This reflects heat from the hot uplifting footwall partially compensating cooling of the HW. Hence, the hanging wall remains closer to conductive thermal equilibrium than it would for a pure burial scenario (e.g., models SB5 and SB6; Fig. 4). In contrast, the greater thickness of uplifting crust in the footwall, compared to the hanging wall, advects heat to shallower model depths during faulting, but still produces rapid cooling during fault motion. Faulting-related cooling is then followed by a short pulse of modest heating (1–2 Myr) after fault motion stops. The heating in this case reflects warming of the hanging wall after faulting, due to the onset of exhumation of the entire crust or lithosphere. Thermochronometer age patterns in EF1 and EF2 are similar to those observed earlier for TF1 and TF2. The AHe, AFT, and ZHe ages are reset during post-faulting exhumation, the ZFT ages in the exhuming footwall record fault-related cooling, and the ZFT ages in the hanging wall are unreset. Interestingly, the evolution of the Moho depth (fixed vs moving) seems to have more impact on the thermochronometer ages than structural position relative to the fault for TF1 and TF2.

In the EF3 and EF4 scenarios, the HW remains fixed during extensional faulting while the FW is exhumed from 15 km to 2.5 km depth (Fig. 6c). Then both the HW and FW are exhumed together to the surface. In this case, heating of the stationary hanging wall in EF3 is clearly visible during and after the period of fault activity in the footwall and followed by slow cooling. The footwall (EF4) shows rapid cooling during faulting, but no period of heating after fault motion stops, as the hanging wall has not cooled like was the case for EF2. Instead, the rate of post-faulting cooling gradually decreases as the final surface particle is exhumed to the surface. Similar to the thrust faulting models TF3 and TF4, only the AHe ages are reset for the hanging wall in EF3, while the rapid cooling during faulting leads to resetting of the AFT, ZHe, and ZFT ages in EF4 (except for ZFT in the FM model variant). As before in TF3, the AHe age in EF4 is reset during post-faulting exhumation.

3.5 Lithospheric delamination-type thermal histories

In models DL1–4, delamination is simulated by removal of the underlying lithospheric mantle and juxtaposition of the asthenosphere against the base of the crust at 50 Ma, followed by 15 km of exhumation over the remainder of the 55 Myr model

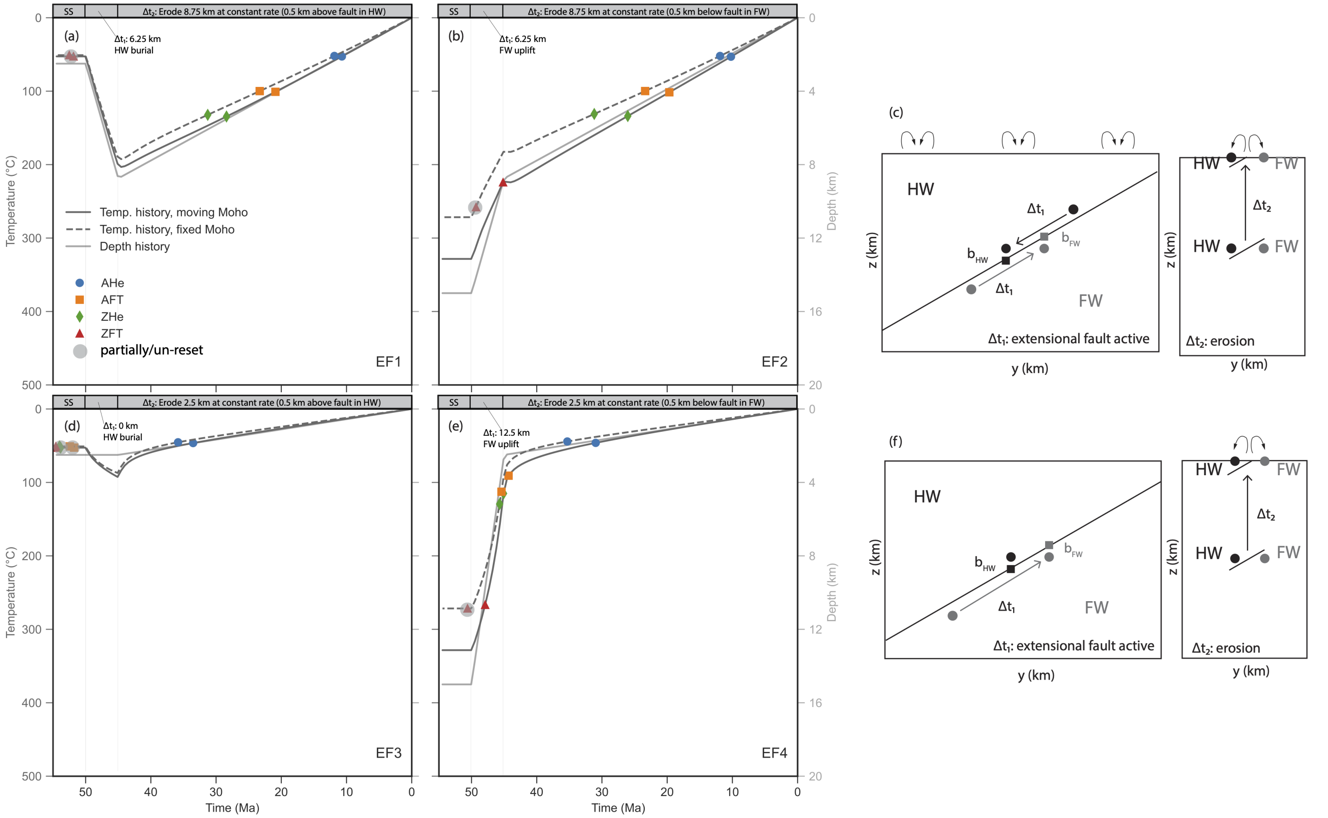

Figure 6. Extensional fault models. (a) and (b) show models EF1 and EF2, respectively, which are hanging wall and footwall thermal and depth histories simulating the fault displacement scenario described in (c) and Table 1: final surface particle paths for particles that are 500 m above the fault in the hanging wall and 500 m below the fault in the footwall, respectively, of an extensional fault dipping 30° that was active over 5 Myr during 50–45 Ma with a partitioning factor of $\lambda = 0.5$ and then exhumed from 8.75 km to the surface. (d) and (e) show models EF3 and EF4, respectively, which are hanging wall and footwall thermal and depth histories for the fault displacement scenario described in (f) and Table 1: same as EF1 and EF2, but with a fixed hanging wall ($\lambda = 1$), and then exhumed from 2.5 km to the surface. Parameters varied in each model are also described in Table 1.

run time. Exhumation styles are similar to scenarios explored in the EE model set, with DL1 involving linear exhumation, and scenarios DL2–4 involving an exponentially decaying rate of erosion with short (2 Myr), medium (10 Myr), and long (50 Myr) exponential decay constants. Each DL model is run with a fixed Moho (FM) and a moving Moho (MM). As for above, the MM scenarios start with a thicker crust (50 km), such that the final Moho depth for FM and MM scenarios is the same, 35 km. For comparison, the individual DL scenarios are plotted against equivalent EE scenarios involving the same magnitude and rate of exhumation, but without lithospheric mantle removal. In this way, it is possible to isolate the influence of bottom-up heating due to the delamination during exhumation of the crust. We note here that Pe values listed below are only for the EE model equivalents to the DL models because the DL models use a high thermal conductivity in the asthenosphere to simulate the thermal effects of mantle convection (Table 2), which biases the calculated Pe values to be too low.

Scenario DL1 involves delamination followed by exhumation of 15 km of crust at a constant rate of 0.3 km/Myr (Pe values: ~ 0.3 (FM), ~ 1.4 (MM); Fig. 7a, b). Cooling ages for both MM (Fig. 7a) and FM (Fig. 7b) are younger than for the EE scenarios without delamination, with cooling not beginning until 5–10 Myr after delamination, despite the continuous rate of exhumation (Fig. 7a). In the MM DL1 scenario, the final surface particle is initially heated by $\sim 10°$ C before beginning its cooling trajectory, resulting in low-temperature thermochronometer ages that are $\sim 1-5$ million years (or up to ~ 16 %) younger than the corresponding EE scenario. However, in the FM DL1 scenario (Fig. 7b), the final surface particle is heated by $\sim 100°$ C before cooling, and so low-temperature thermochronometer ages are $\sim 2-18$ Myr (or up to ~ 36 %) younger compared to the EE scenario (e.g., ZFT age ~ 28 Ma in MM DL1 compared to ~ 42 Ma in the corresponding EE scenario). Clearly, delamination leads to conductive heating from the base of the crust and younger ages in both cases, but the thinner initial crustal thickness in the FM model variant shows a larger effect. This general observation of younger ages for DL scenarios relative to the equivalent EE scenario is common to DL1, DL3, and DL4, in both the FM and MM scenarios (Fig. 7).

The DL2 scenarios, with exponential decay of the exhumation rate over a short period (2 Myr), show rapid cooling immediately following delamination (Fig. 7c, d). The final surface particle is transferred quickly into the uppermost crust, escaping delamination-related heating, despite the middle and lower crust experiencing effective temperature increases of up to 250° C in the first 1–5 Myr of model run time, and reaching peak temperatures that are much higher than in DL1 (see supplementary plots link under Code and data availability). The rapid and significant increase in temperature in the middle and lower crust is a function of both the asthenospheric heating, and the rapid transport of deeper, hotter crust to shallower levels due to the aggressive erosion (maximum Pe values of ~ 6.9 for FM and ~ 32.5 for MM). As a result, there is almost no difference among the DL2 FM and MM scenarios and their equivalent EE scenarios, despite quite different, rapidly evolving geothermal gradients during the 55 Myr model run time.

The remaining DL scenarios, DL3 and DL4, with erosion occurring via medium and long exponential decay constants, respectively, show thermal histories that are intermediate between DL1 and DL2. Similar to DL1, the FM scenarios (Fig. 7f, h) show between 5–10 Myr of heating before reaching peak temperatures and cooling, representing the interplay of surface processes with a dynamic geothermal gradient over the course of the 55 Myr model run time.

Notably, although delamination leads to younger cooling ages in most scenarios (DL1, DL3, DL4), the ages do not record the timing of delamination. Thus it may be quite difficult to determine the timing of such an event from thermochronometer age data alone. In the supplementary results, a more recent delamination scenario is explored, with delamination occurring at 7.5 Ma. In that case, the shallower starting depth of the final surface particle (8 km) prevents full resetting of the zircon thermochronometers, cooling of the particle following delamination is slightly delayed despite active erosion, and the thermal history is largely controlled by exhumation.

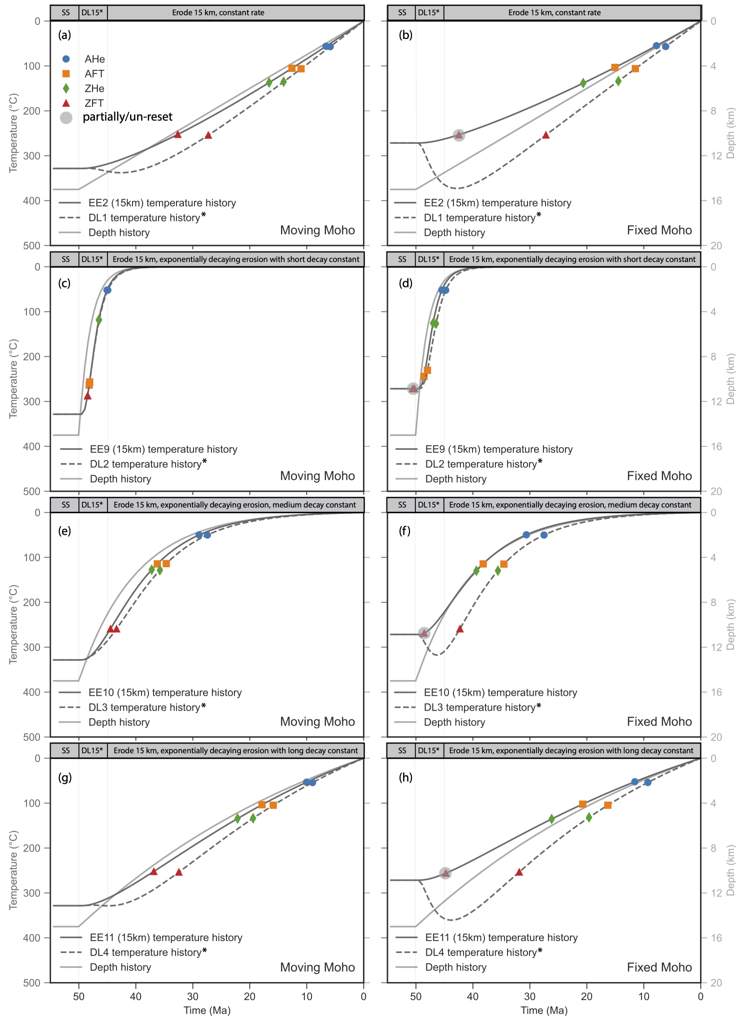

Figure 7. Models exploring delamination (DL) of the sub-continental lithosphere coupled with various erosion styles and erosion triggered at the time of delamination. All models start in a steady state at 55 Ma model time and delamination is triggered instantaneously at 50 Ma model time, followed by 50 Myr of erosion. For comparison, DL models are plotted together with erosional exhumation (EE) models for the same erosion style so that the thermal effect of delamination can be clearly distinguished. DL1 and EE2, in which 15 km of constant erosion follows delamination, are shown with moving Moho (a) and fixed Moho (b); DL2 and EE9, in which 15 km of exponentially decaying erosion (short decay constant) follows delamination, are shown with moving Moho (c) and fixed Moho (d); DL3 and EE10, in which 15 km of exponentially decaying erosion (medium decay constant) follows delamination, are shown with moving Moho (e) and fixed Moho (f), and; DL4 and EE11, in which 15 km of exponentially decaying erosion (long decay constant) follows delamination, are shown with moving Moho (g) and fixed Moho (h). Note that the EE models shown here differ somewhat from those shown in Fig. 3 in that they all involve 15 km of exhumation. See Table 1 for model parameters.

4 Discussion

Above we have explored the thermal histories expected to result from a wide range of erosion, sedimentary burial, dip slip faulting, and sub-continental delamination scenarios. In particular, we have demonstrated that each of these geological processes has the potential to decouple a rock's thermal history from its depth history, and that a rock's low temperature thermochronometer ages may show a strong, weak, asynchronous, or no relationship to geological processes that are known to perturb the crustal thermal field, and that are often assumed to be strongly associated in time and space to thermochronometer age data. For example, only some of the fault scenarios explored showed a close relationship between thermochronometer age and the timing of fault slip. Furthermore, the delamination scenarios showed no relationship between thermochronometer age and timing of delamination.

4.1 Influence of Moho evolution on low-temperature thermal histories

Since low-temperature thermochronology studies are primarily focused on the evolution of the upper crust, the position and evolution of the Moho during the thermal history under investigation is not typically considered. However, in comparing scenarios in which the Moho depth moves down as material is added at the surface (burial), or shallows as material is removed from the surface (exhumation) with equivalent scenarios in which the Moho depth is held fixed, it is clear that the evolution of the Moho depth can influence upper crustal thermal histories. In most of the model scenarios above (with the exception of the SB scenarios), a FM run was compared against a MM run. FM scenarios are considered to be broadly representative of a syn-collisional setting and MM scenarios of a post-tectonic setting (e.g., Wolf et al., 2022), recognizing that this is a simplification and does not address feedback relationships between tectonics and surface processes (Willett, 1999), for example.

The primary observation from these comparisons is that for identical depth histories, the MM or "post-tectonic" models almost always produce younger cooling ages compared to the FM or "collisional" set of models. This pattern of younger MM cooling ages compared to FM cooling ages is consistent among most models run for this study and reflects the higher geothermal gradient in the MM models due to a thicker starting crustal thickness and increased contribution of radiogenic heat production. This produces a higher starting temperature and faster cooling rate during exhumation. In the EE1 case, for example, the starting geothermal gradient of the upper 10 km of crust is only subtly different in the two models at 32° C/km (MM) vs. 29° C/km (FM), yet the resulting ZHe and ZFT ages are 3–7 Myr (or 15–19 %) younger for the MM variant. As would be expected, the difference in predicted age for FM and MM scenarios decreases when samples are very rapidly exhumed, suggesting the influence of Moho position on thermal histories is less important for such settings.

It is also worth noting, however, that the presented FM model variants have a velocity below the crust that is zero, while the velocity of the mantle can also be negative as the result of subduction. This can act to partially compensate the advective heat transport resulting from crustal uplift (e.g., Batt and Braun, 1997) and reduce crustal temperatures. Thus, we include some additional results in the supplementary material under Code and data availability that use a negative mantle velocity with a magnitude equal to the crustal uplift velocity. The predicted ages from these select results are $\sim$3% older on average compared to the case with a zero mantle velocity.

One natural question is whether the differences in age for the MM and FM model variants would be resolvable within the typical uncertainties of apatite and zircon (U-Te)/He or fission-track thermochronometers (10–20 %; e.g., Gautheron et al., 2021). Across all of the models presented in Table 1, the average difference in age between the MM and FM scenarios is ~ 10 %, but numerous cases feature age differences of >20 %. In particular, EE models with larger exhumation magnitudes (EE5–EE8) have predicted ages that differ by more than 20 % for most of the chronometers we modeled (often for all four) with differences as large as ~ 100 % for ZFT in EE8. Despite a lower exhumation magnitude, the AFT and ZHe ages in EE4 also differ by at least 30 % due to the slow cooling prior to a phase of more rapid exhumation. Similarly, the EE model with a constant rate of 15 kilometers of exhumation (EE2, 15 km) has ZHe and ZFT ages that differ by more than 20 %. Age differences are smaller for the EF, TF, and DL scenarios either due to differences in the model kinematics or the effects of heat transfer from delamination, but there are still cases where the age difference is 15–20 %. Thus, we believe that these differences in age due to Moho behavior are indeed significant and should be detectable in measured ages for erosion-dominated scenarios with larger exhumation magnitudes. In addition, mantle subuction would further increase these difference in age between the FM and MM variants, making it more likely that the age differences are detectable in measured ages.

A notable exception to the trend of younger ages for the MM models is for the models of lithospheric mantle delamination (DL models), where little difference in cooling age is observed for both variants. In the DL models, this is the result of two competing factors that to affect the cooling ages. First, crustal temperatures are higher for scenarios where the crustal thickness is larger, due to a larger contribution of radiogenic heat production over the thicker layer. In contrast, however, heating of the middle and upper crust is greater for delamination models when the crustal thickness is lower, due to heat being conducted across a thinner layer. Thus, heating from delamination is greater at upper crustal levels when the crust is thin, and radiogenic heating of the crust is higher when the crust is thick. For example, the final surface particle in the MM variant of model DL1 starts at a higher temperature than its equivalent in the FM version of DL1 ($\sim 330°$ C versus $\sim 270°$ C; Fig. 7a, b). In many of the other models presented earlier, this would result in younger ages for the MM model. However, the thermal effects of delamination have a larger impact on mid-upper crustal depths in the FM model variant, increasing temperatures by $\sim 100°$ C during exhumation, compared to the more modest temperature increase of $\sim 10°$ C for the MM version of DL1. The result of these competing factors is a set of predicted thermochronometer ages for the FM and MM variants that differ by less than 0.5 Myr.

In general, however, the incorporation of the full lithospheric column into thermal history models has shown that the evolution of the Moho can have a strong influence on the thermal structure of the upper crust and should be given consideration when relating rock thermal histories to geological interpretations.

4.2 Relationships between thermal histories and exhumation paths

Although rock cooling in the upper crust can have many causes, it is most commonly considered to be a proxy for rock exhumation (e.g., Reiners et al., 2017), or the approach of a rock towards the Earth's surface. This is because proximity to surface temperatures has a strong control on rock temperature in many, if not most geological settings. The models presented here track both thermal and depth histories of exhumed particles and thus clearly distinguish conditions under which there is a strong relationship between exhumation and thermal history trajectories, and conditions under which they can be decoupled.

Perhaps the most important observation to be made in understanding the relationship between thermal history and exhumation can be found by comparing models EE1 and EE2. These four scenarios (EE1 (FM), EE1 (MM), EE2 (FM) and EE2 (MM)) share an identical, simple exhumation history and final crustal thickness, but produce four different thermal histories, with cooling ages differing by up to 30 %. This outcome emphasizes the fact that even a perfectly known thermal history may be derived from multiple non-unique possible geological histories. In these and all EE models, the shape of the thermal and depth history paths match most closely at depths shallower than ~ 8 km and below $\sim 200°$ C and tend to show deviations at high temperatures and deeper crustal depths. The challenge of non-unique geological histories can be partially mitigated by strategic sampling, such as along vertical profiles and using relationships between elevation and measured age (e.g., Gleadow and Fitzgerald, 1987). Vertical profile sampling to determine exhumation rates, however, can be challenging due to topographic effects on subsurface temperatures, non-vertical sampling, changes in exhumation rate after chronometer closure, and other factors (e.g., Ehlers, 2005). Although data collected in vertical transects may seemingly be difficult to incorporate in 1D software such as T_c1D, it is possible to correct for the effects of surface topography (e.g., Ketcham, 2025), which can provide an option for data interpretation in regions where rates of exhumation may have varied during sample exhumation, for example.

In the models exploring sedimentary burial, the lag time for heating during burial is evident, as is the relative contribution of volumetric heat production to both heating rate and peak temperature in sedimentary basin settings (Fig. 4). In particular, a very fast sedimentation/burial rate could manifest in a thermal history as a slower heating event, regardless of heat production values. In contrast, slower sedimentation rates track burial trajectories more closely.

The fault models presented here show the role of heat conduction in cooling hot fault walls and heating cool ones. The examples presented here, however, likely underestimate the heat transfer produced during faulting since frictional heating is ignored.

The effect of lithospheric delamination is to add heat to the crust, which must dissipate to allow low-temperature thermochronometers to reach closure temperature conditions, moving thermochronometer dates farther from the timing of the delamination event than for an identical erosion scenario that lacks a delamination event.

Rapid exhumation scenarios (the exponential decay scenarios with a short decay time: EE12, DL2) are insensitive to bottom-up heat advection, or position of the Moho, and show the shortest lag times between individual thermochronometers within a given scenario (i.e., overlapping ZFT, ZHe, AFT, and AHe ages, at typical reported errors), and the narrowest difference in thermochronometer ages between moving Moho and fixed Moho scenarios. We infer from this outcome that closely spaced to overlapping ages from multiple thermochronometers are most likely diagnostic of an aggressive, erosional exhumation-dominated system, not a thermal event like delamination or heat transfer by thrust faulting.

4.3 Study limitations

While we argue that a 1D model can help understand how various geological processes are recorded in thermochronological data, it is important to recognize its inherent limitations, and the limitations of how various geological processes have been implemented. The most obvious limitation is the reduction of 3D geological processes to 1D. Subsurface temperatures in the upper crust are affected by surface topography, which can perturb isotherms to depths of roughly 10 km, depending on the exhumation rate and topographic amplitude and wavelength (e.g., Stüwe et al., 1994). This effect is largest in mountainous regions, and although this process can be accounted for to some degree in 1D models by applying a topographic correction (e.g., Ketcham, 2025), such a correction was not applied here and thus care should be used in comparing our results to data from regions characterized by significant topography. In addition, dip-slip fault motion frequently involves both vertical and horizontal motions, resulting in 2D or 3D thermal advection that perturbs the crustal thermal field in a horizontal direction. This effect would be most significant in the results of Sect. 3.3 and 3.4, where the vertical thermal components of dip-slip faulting are simulated for thrust and extensional faults. While the vertical component of motion may be most important for thermochronometer data in rapidly eroding settings (e.g., Whipp et al., 2007), horizontal heat transfer may be more important in regions of active faulting with lower rates of exhumation. Considering both points above, T_c1D would ideally be applied to interpret data from regions with limited topographic relief, moderate to slow rates of exhumation, and little to no active faulting. In other cases, T_c1D may be able to provide estimates of data sensitivity to various geological processes, but a detailed analysis of thermochronometer data may require more sophisticated software such as Pecube (Braun, 2003; Braun et al., 2012).

Our results also do not simulate dynamic erosional responses to geological processes, such as increased erosional exhumation following topographic uplift resulting from lithospheric delamination (Sect. 3.5). It is estimated that removal of the mantle lithosphere would trigger isostatic uplift of the surface by ~ 1 km due to the combination of thermal and density changes. This uplift would likely result a period of increased erosional exhumation that could be simulated with a surface process model, for example. However, surface process models generally require at least two dimensions to simulate hillslope diffusion, and fluvial and glacial erosion processes. It may be possible to link estimated magnitudes of isostatic uplift to a surface process model using T_c1D predictions, but this was not done for the presented results. Additionally, such an exercise would require consideration of topographic effects, as mentioned in the previous paragraph.

The effects of melting and magmatic processes are also not included in the T_c1D results. Partial crustal melting from delamination or magmatic intrusions would be expected to transfer mass, advect heat in the crust, and consume and release heat during melting and crystallization (e.g., Kay and Mahlburg Kay, 1993). This could be locally important in some settings (e.g., Murray et al., 2018) and in some of the model results presented here, such as those for the delamination models or select erosional exhumation scenarios (Sect. 3.1 and 3.5). For instance, present-day reported Moho temperatures greater than 800° C have been correlated with < 10 Ma magmatism in the overlying crust (e.g., Schutt et al., 2018), and temperatures 850–1000° C in the lower crust are expected to cross the wet granite and dry granite solidi (Stern et al., 1975). Since T_c1D does not simulate melting and melt transport, the EE5 MM scenario deviates from geological reality. In cases where crustal melting is a concern, it is possible to plot crustal solidi for various rock compositions in T_c1D to estimate the magnitude of the effects of melting and crystallization.

Finally, we note a few additional limitations that may affect the model predictions for different scenarios. The fixed Moho models are presented as analogs to tectonic scenarios where crustal thickening is balanced by erosion in a syn-tectonic erosional scenario. While this is a reasonable approximation for situations where uplift and erosion are close to in balance, this may not apply for early stages of orogenesis where crustal surface uplift may outpace erosion and thicken the crust (e.g., Beaumont et al., 2000). Additionally, sediment compaction is not modeled for the sedimentary burial and erosional exhumation models (Sect. 3.2). In essence, this means that deposited sediments do not compact, though most sediments can compact by more than 40%, depending on composition (e.g., Athy, 1930). The result is that deposited sediment thicknesses are likely overestimated for the erosional exhumation that follows deposition in the T_c1D models. And finally, the concentration of heat-producing elements in the T_c1D models presented here is constant with depth, rather than decaying. The option for exponential decay of the concentration of heat-producing elements is available in T_c1D, but was not used for the presented results. As a result, lower crustal temperatures may be higher than expected for some scenarios.

5 Conclusions

In conclusion, modeling of the dynamic thermal state of the full lithosphere in 1D allows for testing of expected thermochronometer patterns for a wide range of geological scenarios and parameters. In this contribution, we have modeled a range of erosion, sedimentary burial, fault, and lithospheric delamination scenarios to explore the relationships between those geological processes, the thermal evolution of the lithosphere, and low-temperature thermochronometer ages.

Low-temperature thermochronology studies primarily focus on the evolution of the upper crust, so the position and evolution of the Moho is not typically considered. Here we demonstrated, however, that the evolution of the Moho depth can influence upper crustal thermal histories. For identical depth histories, Moving Moho ("post-tectonic"-type) models almost always produce younger cooling ages compared to Fixed Moho ("syn-collisional"-type) models. This is a reflection of the higher geothermal gradient in the Moving Moho models due to a thicker starting crustal thickness and increased contribution of crustal radiogenic heat production.

Several of the modeled scenarios show a strong relationship between exhumation (depth history) and thermal history trajectories. However, our results have identified several scenarios under which depth and thermal histories can be decoupled, such as during rapid burial of radiogenic sediments, in certain faulting scenarios, and during delamination of the lithospheric mantle. Combined, these results suggest that care should be taken when interepreting low-temperature thermochronometer data, and simple models such as T_c1D may be useful tools to explore data sensitivity to geological processes.

Code and data availability. Results produced here used T_c1D version 0.4.0. Installation instructions can be found on GitHub at https://github.com/HUGG/Tc1D. Model output logs and supplementary plots can be found at https://doi.org/10.23729/fd-dac69f3f-588a-37fd-a348-48670d27985

Appendix A: Thrust and extensional fault kinematics

The kinematics for the thrust faulting (TF) and extensional faulting (EF) models require simulating a 2D (or 3D) process in only 1D. This is done in T_c1D by removing the horizontal component of the fault velocity field and tracking particle depth relative to the reference frame of the hanging wall or footwall, depending upon where the tracking particle is located (Fig. A1. For a

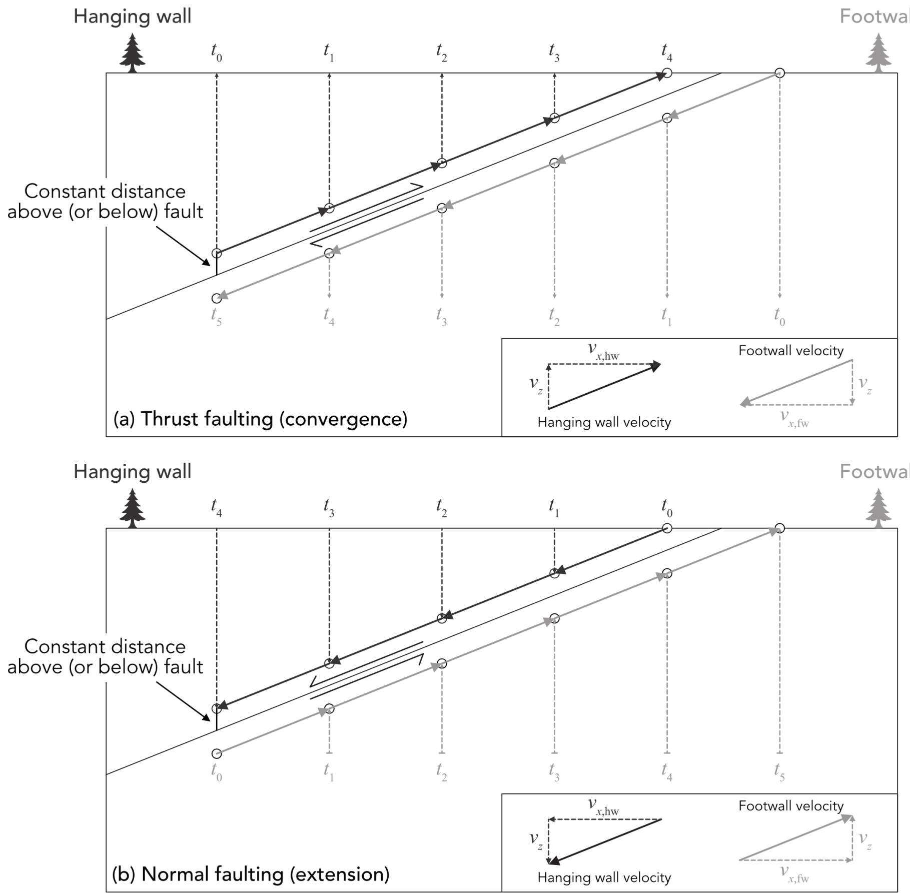

Figure A1. Kinematics of thrust and normal faulting in a reference frame where the fault location is fixed. (a) To an observer standing on the hanging wall of a thrust fault, the fault and tracking particle get shallower with time during fault motion. Thus, to them $v_{x,\mathrm{hw}} = 0$. Conversely, to an observer standing on the footwall, the fault and particle get deeper and $v_{x,\mathrm{fw}} = 0$ in their reference frame. (b) To an observer standing on the hanging wall of a normal fault, the fault and tracking particle get deeper with time during fault motion and again $v_{x,\mathrm{hw}} = 0$ to them. In contrast, the fault and particle get shallower to an observer standing on the footwall, and in their reference frame $v_{x,\mathrm{fw}} = 0$ again. In all cases, v_x is the horizontal velocity, v_z is the vertical velocity, and time increases from t_0 to t_5.

thrust faulting scenario, this reference frame will produce a vertical velocity that moves a tracking particle in the hanging wall upwards at the same velocity as the fault beneath it, maintaining a constant distance above the fault until the particle reaches the surface. This vertical velocity is simply the vertical component of the fault slip velocity. Similarly, a footwall particle will move downwards at the same velocity as the vertical component of fault slip as will the fault above it. Thus, tracking particles will experience different vertical motions, but always maintain a constant vertical distance from the fault during fault motion.

Examples of the vertical velocities tracking particles would experience are shown for the TF and EF models in Fig. A1.

Author contributions. Kellett: Conceptualization, formal analysis, investigation, methodology, validation, visualization, writing (original draft preparation), writing (review and editing). Whipp: Conceptualization, data curation, formal analysis, investigation, methodology, software, validation, visualization, writing (original draft preparation), writing (review and editing)

Competing interests. The authors declare that they have no conflict of interest.

Acknowledgements. Kellett acknowledges funding by Natural Resources Canada's Geomapping for Energy and Minerals-GeoNorth program. This contribution benefited from meaningful discussions with Isabelle Coutand, Scott Jess, Sean Kelly, Karl Lang, and Kelly Thomson.

References

Athy, L. F.: Density, Porosity, and Compaction of Sedimentary Rocks, AAPG Bulletin, 14, 1–24, https://doi.org/10.1306/3D93289E-16B1-11D7-8645000102C1865D, 1930.

Bao, X., Eaton, D. W., and Guest, B.: Plateau Uplift in Western Canada Caused by Lithospheric Delamination along a Craton Edge, Nature Geoscience, 7, 830–833, https://doi.org/10.1038/ngeo2270, 2014.

Batt, G. E. and Braun, J.: On the Thermomechanical Evolution of Compressional Orogens, Geophysical Journal International, 128, 364–382, 1997.

Beaumont, C., Kooi, H., and Willett, S. D.: Coupled Tectonic-Surface Process Models with Applications to Rifted Margins and Collisional Orogens, in: Geomorphology and Global Tectonics, edited by Summerfield, M. A., p. 367, John Wiley \& Sons, Ltd., West Sussex, U.K., 2000.

Bezada, M. J., Humphreys, E. D., Davila, J., Carbonell, R., Harnafi, M., Palomeras, I., and Levander, A.: Piecewise Delamination of Moroccan Lithosphere from beneath the Atlas Mountains, Geochemistry, Geophysics, Geosystems, 15, 975–985, https://doi.org/10.1002/2013GC005059, 2014.

Bidgoli, T. S., Amir, E., Walker, J. D., Stockli, D. F., Andrew, J. E., and Caskey, S. J.: Low-Temperature Thermochronology of the Black and Panamint Mountains, Death Valley, California: Implications for Geodynamic Controls on Cenozoic Intraplate Strain, Lithosphere, https://doi.org/10.1130/L406.1, 2015.

Braun, J.: Pecube: A New Finite-Element Code to Solve the 3D Heat Transport Equation Including the Effects of a Time-Varying, Finite Amplitude Surface Topography, Computers \& Geosciences, 29, 787–794, 2003.

Braun, J., van der Beek, P., Valla, P. G., Robert, X., Herman, F., Glotzbach, C., Pedersen, V., Perry, C., Simon-Labric, T., and Prigent, C.: Quantifying Rates of Landscape Evolution and Tectonic Processes by Thermochronology and Numerical Modeling of Crustal Heat Transport Using PECUBE, Tectonophysics, 524\textendash525, 1–28, 2012.

Dai, J., Wang, C., Hourigan, J., Li, Z., and Zhuang, G.: Exhumation History of the Gangdese Batholith, Southern Tibetan Plateau: Evidence from Apatite and Zircon (U-Th)/He Thermochronology, The Journal of Geology, 121, 155–172, https://doi.org/10.1086/669250, 2013.

Drew, S. T., Ducea, M. N., and Schoenbohm, L. M.: Mafic Volcanism on the Puna Plateau, NW Argentina: Implications for Lithospheric Composition and Evolution with an Emphasis on Lithospheric Foundering, Lithosphere, 1, 305–318, https://doi.org/10.1130/L54.1, 2009.

Ducea, M. N.: Fingerprinting Orogenic Delamination, Geology, 39, 191–192, https://doi.org/10.1130/focus022011.1, 2011.

Ehlers, T. A.: Crustal Thermal Processes and the Interpretation of Thermochronometer Data, in: Low-Temperature Thermochronology: Techniques, Interpretations and Applications, pp. 315–350, Mineralogical Society of America, 2005.

Flowers, R. M., Ketcham, R. A., Shuster, D. L., and Farley, K. A.: Apatite (U-Th)/He Thermochronometry Using a Radiation Damage Accumulation and Annealing Model, Geochimica et Cosmochimica Acta, 73, 2347–2365, 2009.

Flowers, R. M., Farley, K. A., and Ketcham, R. A.: A Reporting Protocol for Thermochronologic Modeling Illustrated with Data from the Grand Canyon, Earth and Planetary Science Letters, 432, 425–435, https://doi.org/10.1016/j.epsl.2015.09.053, 2015.

Fraser, K. I., Enkelmann, E., Jess, S., Gilbert, H., and Grieco, R.: Resolving the Cenozoic History of Rock Exhumation Along the Central Rocky Mountain Trench Using Apatite Low-Temperature Thermochronology, Tectonics, 40, e2021TC006 847, https://doi.org/10.1029/2021TC006847, 2021.

Gallagher, K.: Transdimensional Inverse Thermal History Modeling for Quantitative Thermochronology, Journal of Geophysical Research: Solid Earth, 117, https://doi.org/10.1029/2011JB008825, 2012.

Garzione, C. N., Molnar, P., Libarkin, J. C., and MacFadden, B. J.: Rapid Late Miocene Rise of the Bolivian Altiplano: Evidence for Removal of Mantle Lithosphere, Earth and Planetary Science Letters, 241, 543–556, https://doi.org/http://dx.doi.org/10.1016/j.epsl.2005.11.026, 2006.

Garzione, C. N., Hoke, G. D., Libarkin, J. C., Withers, S., MacFadden, B., Eiler, J., Ghosh, P., and Mulch, A.: Rise of the Andes, Science, 320, 1304–1307, 2008.

Gautheron, C., Pinna-Jamme, R., Derycke, A., Ahadi, F., Sanchez, C., Haurine, F., Monvoisin, G., Barbosa, D., Delpech, G., Maltese, J., Sarda, P., and Tassan-Got, L.: Technical Note: Analytical Protocols and Performance for Apatite and Zircon (U–Th) / He Analysis on Quadrupole and Magnetic Sector Mass Spectrometer Systems between 2007 and 2020, Geochronology, 3, 351–370, https://doi.org/10.5194/gchron-3-351-2021, 2021.

Gleadow, A. J. W. and Fitzgerald, P. G.: Uplift History and Structure of the Transantarctic Mountains: New Evidence from Fission Track Dating of Basement Apatites in the Dry Valleys Area, Southern Victoria Land, Earth and Planetary Science Letters, 82, 1–14, https://doi.org/10.1016/0012-821X(87)90102-6, 1987.

Göğüş, O. H. and Ueda, K.: Peeling Back the Lithosphere: Controlling Parameters, Surface Expressions and the Future Directions in Delamination Modeling, Journal of Geodynamics, 117, 21–40, https://doi.org/10.1016/j.jog.2018.03.003, 2018.

Guenthner, W. R.: Implementation of an Alpha Damage Annealing Model for Zircon (U-Th)/He Thermochronology With Comparison to a Zircon Fission Track Annealing Model, Geochemistry, Geophysics, Geosystems, 22, e2019GC008 757, https://doi.org/10.1029/2019GC008757, 2021.

Guenthner, W. R., Reiners, P. W., Ketcham, R. A., Nasdala, L., and Giester, G.: Helium Diffusion in Natural Zircon: Radiation Damage, Anisotropy, and the Interpretation of Zircon (U-Th)/He Thermochronology, American Journal of Science, 313, 145–198, https://doi.org/10.2475/03.2013.01, 2013.

Kay, R. W. and Mahlburg Kay, S.: Delamination and Delamination Magmatism, Tectonophysics, 219, 177–189, https://doi.org/10.1016/0040-1951(93)90295-U, 1993.

Ketcham, R. A.: Forward and Inverse Modeling of Low-Temperature Thermochronometry Data, in: Low-Temperature Thermochronology: Techniques, Interpretations and Applications, pp. 275–314, Mineralogical Society of America, 2005.

Ketcham, R. A.: Technical Note: Incorporating Topographic Deflection Effects into Thermal History Modelling, EGUsphere, pp. 1–14, https://doi.org/10.5194/egusphere-2025-901, 2025.

Ketcham, R. A., Donelick, R. A., and Carlson, W. D.: Variability of Apatite Fission-Track Annealing Kinetics; III, Extrapolation to Geological Time Scales, American Mineralogist, 84, 1235–1255, 1999.

Ketcham, R. A., Donelick, R. A., and Donelick, M. B.: AFTSolve: A Program for Multi-Kinetic Modeling of Apatite Fission-Track Data, Geological Materials Research, 2, 1–32, 2000.

Ketcham, R. A., Mora, A., and Parra, M.: Deciphering Exhumation and Burial History with Multi-Sample down-Well Thermochronometric Inverse Modelling, Basin Research, 30, 48–64, https://doi.org/10.1111/bre.12207, 2018.

Lock, J. and Willett, S.: Low-Temperature Thermochronometric Ages in Fold-and-Thrust Belts, Tectonophysics, 456, 147–162, 2008.

Mansour, J., Giordani, J., Moresi, L., Beucher, R., Kaluza, O., Velic, M., Farrington, R., Quenette, S., and Beall, A.: Underworld2: Python Geodynamics Modelling for Desktop, HPC and Cloud, Journal of Open Source Software, 5, 1797, https://doi.org/10.21105/joss.01797, 2020.

McMillan, M. and Schoenbohm, L. M.: Diverse Styles of Lithospheric Dripping: Synthesizing Gravitational Instability Models, Continental Tectonics, and Geologic Observations, Geochemistry, Geophysics, Geosystems, 24, e2022GC010 488, https://doi.org/10.1029/2022GC010488, 2023.

McQuarrie, N. and Ehlers, T. A.: Influence of Thrust Belt Geometry and Shortening Rate on Thermochronometer Cooling Ages: Insights from Thermokinematic and Erosion Modeling of the Bhutan Himalaya, Tectonics, 34, 1055–1079, 2015.

McQuarrie, N., Ehlers, T. A., Law, R. D., Thigpen, J. R., Merschat, A. J., and Stowell, H. H.: Techniques for Understanding Fold-and-Thrust Belt Kinematics and Thermal Evolution, in: Linkages and Feedbacks in Orogenic Systems, Geological Society of America, ISBN 978-0-8137-1213-0, 2017.

Murray, K. E., Braun, J., and Reiners, P. W.: Toward Robust Interpretation of Low-Temperature Thermochronometers in Magmatic Terranes, Geochemistry, Geophysics, Geosystems, 19, 3739–3763, https://doi.org/10.1029/2018GC007595, 2018.

Oxburgh, E. R. and Turcotte, D. L.: Thermal Gradients and Regional Metamorphism in Overthrust Terrains with Special Reference to the Eastern Alps, Schweizerische mineralogische und petrographische Mitteilungen, 54, https://doi.org/10.5169/seals-42213, 1974.

Rahn, M. K., Brandon, M. T., Batt, G. E., and Garver, J. I.: A Zero-Damage Model for Fission-Track Annealing in Zircon, American Mineralogist, 89, 473–484, https://doi.org/10.2138/am-2004-0401, 2004.

Reiners, P. W., Carlson, R. W., Renne, P. R., Cooper, K. M., Granger, D. E., McLean, N. M., and Schoene, B.: Geochronology and Thermochronology, John Wiley & Sons, 2017.

Salles, T. and Hardiman, L.: Badlands: An Open-Source, Flexible and Parallel Framework to Study Landscape Dynamics, Computers & Geosciences, 91, 77–89, https://doi.org/10.1016/j.cageo.2016.03.011, 2016.

Schutt, D. L., Lowry, A. R., and Buehler, J. S.: Moho Temperature and Mobility of Lower Crust in the Western United States, Geology, 46, 219–222, https://doi.org/10.1130/G39507.1, 2018.

Stern, C. R., Huang, W.-L., and Wyllie, P. J.: Basalt-Andesite-Rhyolite-H2O: Crystallization Intervals with Excess H2O and H2O-undersaturated Liquidus Surfaces to 35 Kilobars, with Implications for Magma Genesis, Earth and Planetary Science Letters, 28, 189–196, https://doi.org/10.1016/0012-821X(75)90226-5, 1975.

Stockli, D. F.: Application of Low-Temperature Thermochronometry to Extensional Tectonic Settings, in: Low-Temperature Thermochronology: Techniques, Interpretations and Applications, pp. 411–448, Mineralogical Society of America, 2005.

Stüwe, K., White, L., and Brown, R.: The Influence of Eroding Topography on Steady-State Isotherms; Application to Fission Track Analysis, Earth and Planetary Science Letters, 124, 63–74, 1994.

Tagami, T., Galbraith, R. F., Yamada, R., and Laslett, G. M.: Revised Annealing Kinetics of Fission Tracks in Zircon and Geological Implications, in: Advances in Fission-Track Geochronology: A Selection of Papers Presented at the International Workshop on Fission-Track Dating, Ghent, Belgium, 1996, edited by van den Haute, P. and de Corte, F., pp. 99–112, Springer Netherlands, Dordrecht, ISBN 978-94-015-9133-1, https://doi.org/10.1007/978-94-015-9133-1_8, 1998.

Turcotte, D. L. and Schubert, G.: Geodynamics, Cambridge University Press, Cambridge, UK, 3rd edn., 2014.

van der Beek, P., Andriessen, P., and Cloetingh, S.: Morphotectonic Evolution of Rifted Continental Margins: Inferences from a Coupled Tectonic-Surface Processes Model and Fission Track Thermochronology, Tectonics, 14, 406–421, https://doi.org/10.1029/94TC02445, 1995.

Whipp, D. M.: Tc1D: A 1D Thermal and Thermochronometer Age Prediction Model, https://doi.org/10.5281/zenodo.7124271, 2022.

Whipp, D. M., Ehlers, T. A., Blythe, A. E., Huntington, K. W., Hodges, K. V., and Burbank, D. W.: Plio-Quaternary Exhumation History of the Central Nepalese Himalaya: 2. Thermo-kinematic and Thermochronometer Age Prediction Model, Tectonics, 26, 2007.

Whipp, D. M., Kellett, D. A., Coutand, I., and Ketcham, R. A.: Short Communication: Modeling Competing Effects of Cooling Rate, Grain Size, and Radiation Damage in Low-Temperature Thermochronometers, Geochronology, 4, 143–152, https://doi.org/10.5194/gchron-4-143-2022, 2022.

Whipp, D. M., Gérard, B., Laaksonen, S., and Kellett, D. A.: Technical Note: T_c1D - a 1D Thermal and Thermochronometer Age Prediction Model, EGUsphere, pp. 1–25, https://doi.org/10.5194/egusphere-2026-2514, 2026.

Willett, S. D.: Orogeny and Orography; the Effects of Erosion on the Structure of Mountain Belts, Journal of Geophysical Research, B, Solid Earth and Planets, 104, 28,957–28,982, 1999.

Wolf, S. G., Huismans, R. S., Braun, J., and Yuan, X.: Topography of Mountain Belts Controlled by Rheology and Surface Processes, Nature, pp. 1–6, https://doi.org/10.1038/s41586-022-04700-6, 2022.

Zandt, G., Gilbert, H., Owens, T. J., Ducea, M., Saleeby, J., and Jones, C. H.: Active Foundering of a Continental Arc Root beneath the Southern Sierra Nevada in California, Nature, 431, 41–46, https://doi.org/10.1038/nature02847, 2004.